

¹ Susceptible host dynamics explain pathogen resilience to
² perturbations
³

⁴
⁵ Sang Woo Park, . . . , Sarah Cobey

⁶ Abstract

⁷ Major priority for epidemiological research in the time of anthropogenic change is
⁸ understanding how infectious disease dynamics respond to perturbations. Interven-
⁹ tions to slow the spread of SARS-CoV-2 significantly disrupted the transmission
¹⁰ of other human pathogens. As interventions lifted, whether and when respiratory
¹¹ pathogens would eventually return to their pre-pandemic dynamics remains to be
¹² answered. To address this gap, we develop a framework for estimating pathogen re-
¹³ silience based on how fast epidemic patterns return to their pre-pandemic, endemic
¹⁴ dynamics. Our analysis suggests that some pathogens may have settled to endemic
¹⁵ cycles that are different from their pre-pandemic patterns. Finally, we show that
¹⁶ the replenishment rate of the susceptible pool is a key determinant of pathogen re-
¹⁷ silience. Our framework offers a novel perspective to characterizing the dynamics of
¹⁸ endemic pathogens and their responses to SARS-CoV-2 interventions. [SWP: Need
¹⁹ to emphasize broader implications.]

Non-pharmaceutical interventions (NPIs) to slow the spread of SARS-CoV-2 disrupted the transmission of other human respiratory pathogens, adding uncertainties to their future epidemic dynamics and the overall public health burden [1]. As interventions lifted, large heterogeneities in outbreak dynamics were observed across different pathogens in different countries, with some pathogens exhibiting earlier resurgences than others [2, 3, 4]. Heterogeneities in the overall reduction in transmission and the timing of re-emergence likely reflect differences in NPI patterns, pathogen characteristics, immigration/importation from other countries, and pre-pandemic pathogen dynamics [5]. Therefore, comparing the differential impact of the pandemic NPIs across pathogens can provide unique opportunities to learn about underlying pathogen characteristics, such as their transmissibility or duration of immunity, from heterogeneities in re-emergence patterns [6].

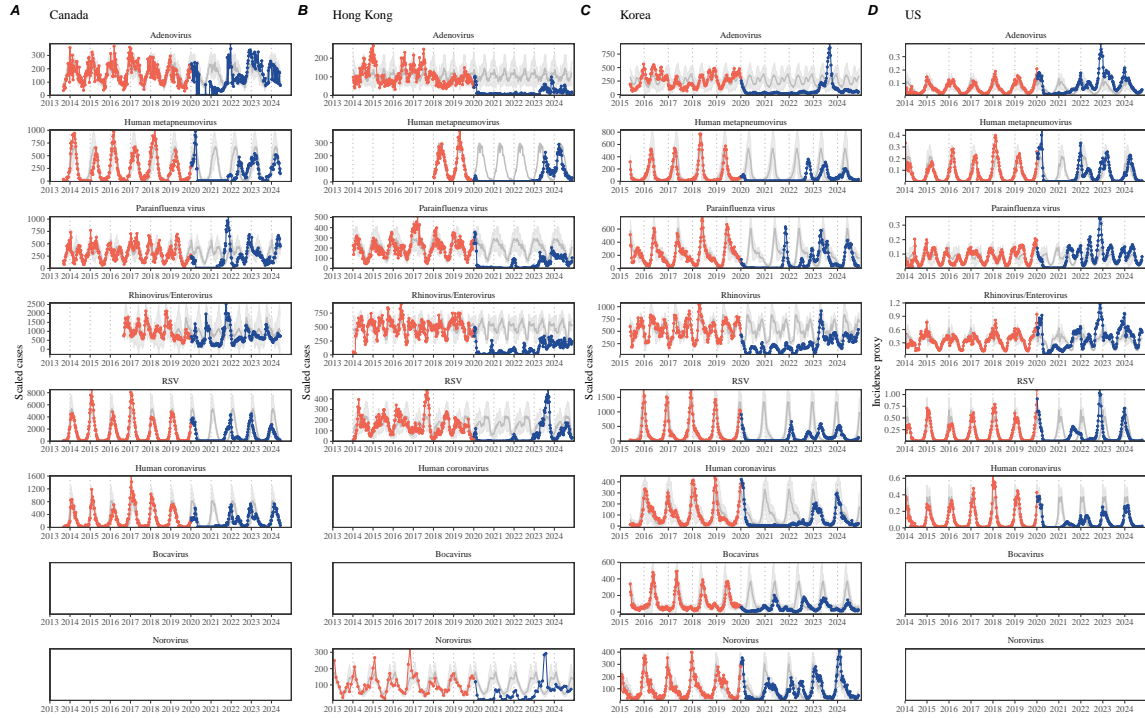


Figure 1: Observed heterogeneity in responses to COVID-19 pandemic across respiratory pathogens and norovirus in (A) Canada, (B) Hong Kong, (C) Korea, and (D) US. Red points and lines represent data before 2020. Blue points and lines represent data since 2020. Gray lines and shaded regions represent the mean seasonal patterns and corresponding 95% confidence intervals based on the observed outbreak patterns before 2020.

Even though more than five years have passed since the emergence of SARS-CoV-2, we still observe persistent changes in pathogen dynamics following the pandemic NPIs: for example, compared to pre-pandemic, seasonal patterns, human metapneumovirus and bocavirus in Korea are circulating at lower levels, whereas RSV in Korea

36 seem to exhibit different seasonality (Figure 1). These observations suggest a possi-
37 bility for a fundamental change in pathogen dynamics following the pandemic NPIs,
38 which can be driven by permanent shift in either human behavior or population-level
39 immunity [7, 8]. Moreover, the possibility of a long-lasting impact of the pandemic
40 NPIs pose an important question for future infectious disease dynamics: can we pre-
41 dict whether and when other respiratory pathogens will eventually return to their
42 pre-pandemic dynamics?

43 So far, the majority of epidemiological analyses of respiratory pathogens in the
44 context of the pandemic NPIs have focused on characterizing the timing of rebound
45 [1, 9, 5]. Instead, we seek to characterize how fast a pathogen returns to its pre-
46 pandemic dynamics. These two concepts have subtle but important differences: for
47 example, it took more than 3 years for human metapneumovirus to rebound in Hong
48 Kong but the observed epidemic patterns in 2024 are similar to pre-pandemic seasonal
49 means, suggesting a rapid return to pre-pandemic dynamics following a perturbation
50 (Figure 1). Measuring this rate of return is particularly useful because it allows us
51 to quantify the ecological resilience of a host-pathogen system [10, 11, 12, 13].

52 In this study, we lay out theoretical and statistical approaches to characterizing
53 the resilience of a host-pathogen system based on how fast the system recovers from
54 perturbation. We begin by laying out a few representative scenarios that capture
55 the potential impact of COVID-19 interventions on endemic pathogen dynamics and
56 illustrate how resilience can be measured by comparing the pre- and post-pandemic
57 dynamics of susceptible and infected hosts. In practice, information on susceptible
58 hosts is often unavailable, making this theoretical approach infeasible. Instead, we
59 utilize a mathematical technique to reconstruct empirical attractors from the data
60 [14], which allows us to measure the rate at which the host-pathogen system ap-
61 proaches this empirical attractor after a perturbation; this rate corresponds to the
62 resilience of the host-pathogen system. We use this method to analyze pathogen
63 surveillance data for respiratory and non-respiratory pathogens from Canada, Hong
64 Kong, Korea, and US. Finally, we show that susceptible host dynamics explain vari-
65 ation in pathogen resilience.

66 Conceptual introduction to pathogen resilience

67 In classical ecological literature, resilience of an ecological system is measured by
68 the rate at which the system returns to its reference state following a perturbation
69 [10, 11, 12, 13]. This rate corresponds to the largest real part of the eigenvalues of
70 the linearized system near equilibrium—here, we refer to this value as the *intrinsic*
71 resilience of the system, which represents the expected rate of return from perturbed
72 states. However, respiratory pathogens often exhibit seasonal variation in transmis-
73 sion, meaning that the intrinsic resilience of a host-pathogen system varies across
74 season. Nonetheless, we can still measure the *empirical* resilience of a host-pathogen
75 system by looking at how fast the system returns to the pre-pandemic, endemic

76 dynamics after interventions are lifted.

77 As an example, consider an intervention that reduce transmission by 50% for 6
78 months starting in 2020, which causes epidemic patterns to deviate from its original
79 stable annual cycle for a short period of time and eventually come back (Figure 2A).
80 To measure the empirical resilience of this system, we first need to be able to measure
81 the distance from its pre-pandemic attractor. There are many different ways we can
82 measure the distance from attractor, but for illustrative purposes, we choose one of
83 the most parsimonious approach: that is, we look at how the susceptible (S) and
84 infected (I) populations change over time and measure the distance on the SI phase
85 plane (Figure 2B). In this simple case, the locally estimated scatterplot smoothing
86 (LOESS) fit indicates that the distance from attractor decreases linearly on average
87 (Figure 2C). Furthermore, the overall rate of return matches the intrinsic resilience
88 of the seasonally unforced system (Figure 2C).

89 Alternatively, NPIs can permanently change our behavior and have persisting
90 impact on the pathogen dynamics; as an example, we consider a scenario in which a
91 10% reduction in transmission persists even after the NPIs are lifted (Figure 2D–F).
92 In such cases, we cannot know whether the pathogen will return to its original cycle
93 or a different cycle until many years have passed after the NPIs are lifted, meaning
94 that we cannot measure the distance against the new attractor that the system will
95 eventually approach. Nonetheless, we can still measure the distance against the orig-
96 inal, pre-pandemic attractor and ask how the distance changes over time (Figure 2E).
97 The LOESS fit suggests that the distance from the attractor will initially decrease
98 exponentially on average (equivalently, linearly on a log scale) and eventually plateau
99 (Figure 2F). Here, a permanent 10% reduction in transmission rate slows down the
100 system, which causes the distance from the attractor to decrease at a slower rate
101 (Figure 2F) than it would have otherwise in the absence of permanent transmission
102 reduction (Figure 2C). This example shows that resilience is not necessarily an in-
103 trinsic property of a specific pathogen. Instead, pathogen resilience is a property of
104 a specific attractor that a host-pathogen system approaches, which depends on both
105 pathogen and host characteristics.

106 Finally, transient phenomena can also complicate the picture (Figure 2G–I). For
107 example, a stage-structured model for RSV initially exhibits a stable annual cycle,
108 but perturbations from NPIs cause the epidemic to exhibit biennial cycles (Figure
109 2G). Despite this biennial cycle, we see that the system eventually approaches the
110 original pre-pandemic attractor (Figure 2H), suggesting that this biennial cycle is a
111 transient phenomenon. The LOESS fit indicates that the distance from the attractor
112 will initially decrease exponentially at a rate that is consistent with the intrinsic
113 resilience of the seasonally unforced system, but the rate of decrease slows down
114 as the epidemic exhibits a biennial cycle (Figure 2I). In classical ecological theory,
115 this behavior is also referred to as a ghost attractor, which causes long transient
116 dynamics and slow transitions [15]. As we show in Supplementary Figure S1, strong
117 seasonal forcing in transmission can also lead to transient phenomena for a simple
118 SIRS model, causing a slowing down of the system.

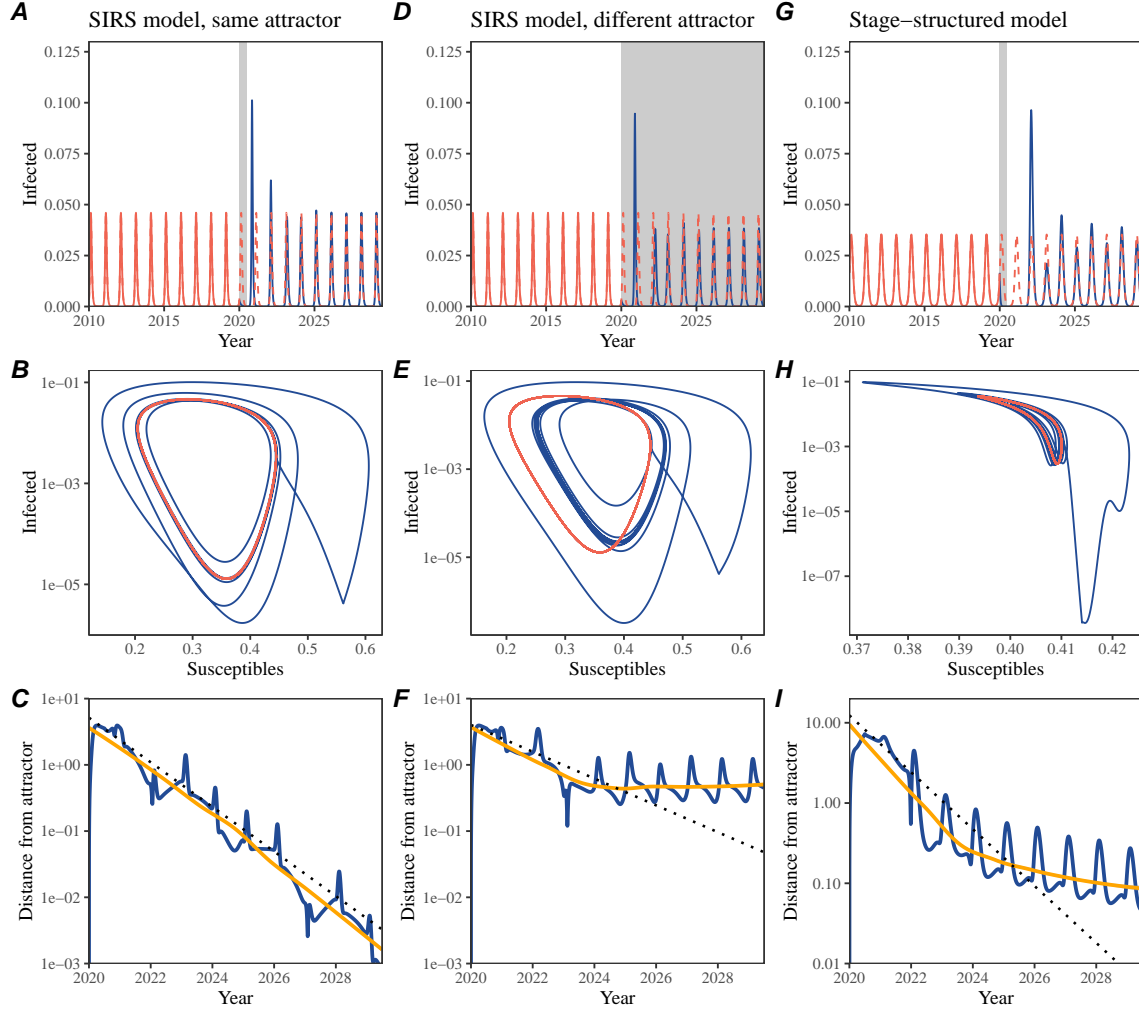


Figure 2: Conceptual framework for measuring pathogen resilience following NPIs across different scenarios. (A, D, G) Simulated epidemic trajectories across various models. Red and blue solid lines represent epidemic dynamics before and after interventions are introduced, respectively. Red dashed lines represent counterfactual epidemic dynamics in the absence of interventions. Gray regions indicate the duration of interventions. (B, E, H) Phase plane representation of the corresponding model. Red and blue solid lines represent epidemic trajectories on an SI phase plane before and after interventions are introduced, respectively. (C, F, I) Changes in logged distance from attractor over time. Blue lines represent the logged distance from attractor. Orange lines represent the locally estimated scatterplot smoothing (LOESS) fits to the logged distance from attractor. Dotted lines are superimposed as a comparison to have the same slope as the intrinsic resilience of the seasonally unforced system.

119 In Supplementary Materials, we also explore measuring the resilience of a two-

120 strain host-pathogen system: when the dynamics two strains (or two pathogens) are
121 coupled through cross immunity, we would expect the entire system to be character-
122 ized by a single resilience value (rather than having two separate resilience for each
123 strain). Simulations from a simple two-strain system illustrate that separate anal-
124 yses of individual strain dynamics (e.g., RSV A vs B) and a joint analysis of total
125 infections (e.g., total RSV infections) yield identical resilience estimates, confirming
126 our expectation (Supplementary Figure S2, 3). Analogous to a single system, strong
127 seasonal forcing in transmission can cause the system to slow down through transient
128 phenomena (Supplementary Figure S4).

129 These observations indicate three possibilities. First, we can directly estimate
130 the empirical resilience of a host-pathogen system by looking at how fast the system
131 approaches a pre-pandemic attractor, provided that we can measure the distance
132 from attractor. The empirical approach to estimating pathogen resilience is partic-
133 ularly convenient because it does not require us to know the true underlying model.
134 As we show in Supplementary Figure S5, estimating the intrinsic resilience from fit-
135 ting standard compartmental models can lead to biased estimates, especially under
136 model misspecification. Second, resilience estimates allow us to make phenomenolog-
137 ical predictions about the dynamics of a host-pathogen system following a perturba-
138 tion: assuming that the distance from the attractor will decrease exponentially over
139 time, we can obtain a ballpark estimate for when the system will reach an attractor.
140 Finally, deviation from an exponential decrease in the distance from attractor can
141 provide information about whether the system has reached an alternative attractor,
142 or a ghost attractor, that is different from the original, pre-pandemic attractor. These
143 alternative attractors may reflect continued perturbations from permanent changes
144 in transmission patterns as well as changes in immune landscapes.

145 **Inferring pathogen resilience from real data**

146 Based on these observations, we now set out to infer pathogen resilience from real
147 data. Here, we briefly lay out our approach to estimating pathogen resilience from
148 real data (Figure 3). We then test this approach against simulations and apply it to
149 real data.

150 So far, we focused on simple examples that assume a constant transmission re-
151 duction. However, in practice, the impact of NPIs on pathogen transmission is
152 likely more complex (Figure 3A), reflecting introduction and relaxation of various
153 intervention strategies. These complexities can lead to longer delays between the
154 introduction of NPIs and pathogen re-emergence as well as temporal variation in
155 outbreak sizes (Figure 3B): in this example, continued transmission reduction from
156 NPIs limits the size of the first outbreak in 2021 following the emergence, allowing
157 for a larger outbreak in 2022 when NPIs are further relaxed.

158 Previously, we relied on the dynamics of susceptible and infected hosts to compute
159 the distance from attractor (Figure 2), but information on susceptible hosts are

often not available in practice. In addition, uncertainties in case counts due to observation error as well as the possibility of complex, multiannual attractor adds challenges to measuring the distance from attractor. To address these challenges, we first reconstruct an empirical attractor by utilizing Takens' theorem, which states that an attractor of a nonlinear multidimensional system can be mapped onto a delayed embedding [14]. Here, we use delayed copies of logged values of pre-pandemic cases $C(t)$ (Figure 3C) to reconstruct the attractor:

$$\langle \log(C(t) + 1), \log(C(t - \tau) + 1), \dots, \log(C(t - (M - 1)\tau) + 1) \rangle, \quad (1)$$

where the delay τ and embedding dimension M are determined based on autocorrelations and false nearest neighbors, respectively [16, 17]. We then apply the same delay and embedding dimensions to the entire time series to determine the position on a multi-dimensional state space (Figure 3D), which allows us to measure the nearest neighbor distance between the current state of the system and the empirical attractor (Figure 3E). In principle, we can quantify how fast this distance decreases by fitting a linear regression on a log scale, where the slope of the linear regression corresponds to pathogen resilience. As we show in Supplementary Figure S6, overall temporal variations in the distance from attractor, especially the observed rate of decrease, appear robust to choices about embedding delays and dimensions; we note that using longer delays and higher dimensions tend to smooth out temporal variations in the distance from attractor.

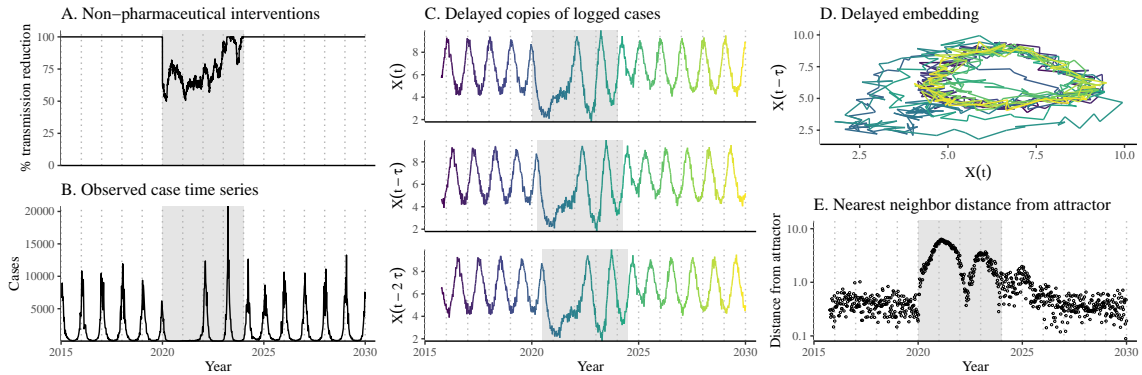


Figure 3: A schematic diagram explaining how pathogen resilience can be inferred from real data. (A) A realistic example of a synthetic NPI, represented by a relative reduction in transmission. (B) The impact of the synthetic NPI on epidemic dynamics simulated using a stochastic SIRS model. (C) Generating delayed copies of the logged time series allows us to obtain an embedding. (D) Two dimensional representation of an embedding. (E) Delayed embedding allows us to calculate the nearest neighbor distance from the empirical attractor, which is determined based on the pre-pandemic time series. This distance time series can be used to infer pathogen resilience by fitting a linear regression after choosing an appropriate window for regression.

179 Complex changes in the distance from attractor suggest that estimating pathogen
180 resilience from linear regression will likely be sensitive to our choice of fitting windows
181 for the regression. In Supplementary Materials, we explore an automated window
182 selection criteria for linear regression and test it against randomized, stochastic sim-
183 ulations across a wide range of realistic NPI shapes. We find that resilience estimates
184 based on the automated window selection criteria are moderately correlated (0.48)
185 with the intrinsic resilience of the post-NPI attractor (Supplementary Figure S7). In
186 contrast, a naive approach that uses the entire time series, starting from the peak
187 distance, only gives a correlation of 0.09 and consistently underestimates the intrinsic
188 resilience (Supplementary Figure S7).

189 Now, we apply this approach to pathogen surveillance data presented in Figure
190 1. For each time series, we apply Takens' theorem independently to reconstruct the
191 empirical attractor and obtain the corresponding time series of distance from attrac-
192 tors (Supplementary Figure S8 for the distance time series and linear regression fits).
193 Then, we use the automated window selection criteria to fit a linear regression and
194 estimate the empirical resilience for each pathogen in each country. For most res-
195 piratory pathogens, resilience estimates fall between 0.4/year and 1.8/year (Figure
196 4A), with the exception of Rhinovirus in the US (0.066/year; 95% CI: 0.018/year–
197 0.113/year) and Bocavirus in Korea (0.087/year; 95% CI: 0.023/year–0.151/year).
198 Excluding these exceptions, the mean resilience of common respiratory pathogens is
199 0.974/year (95% CI: 0.784/year–1.16/year). As a reference, this is \approx 7 times higher
200 than the intrinsic resilience of pre-vaccination measles dynamics (\approx 0.13/year). Fi-
201 nally, resilience estimates for norovirus appears to be comparable to the intrinsic
202 resilience of measles: 0.119/year (95%CI: 0.004/year–0.233/year) for Korea and
203 0.385/year (95% CI: 0.167/year–0.603/year). A simple ANOVA shows that there
204 are significant differences in resilience estimates across countries ($p < 0.036$) and
205 pathogens ($p < 0.030$).

206 Using resilience estimates, we now predict when each pathogen will return to
207 their original pre-pandemic cycles. Specifically, we extend our linear regression fits
208 to distance-from-attractor time series and ask when the predicted regression line
209 will cross a threshold value, which we set to a mean of pre-pandemic distances. We
210 predict that a return to pre-pandemic cycles would be imminent for most pathogens
211 (Figure 4B; see Supplementary Figure S9 for a zoomed out version). In addition, we
212 also predict that many pathogens should have already returned to their pre-pandemic
213 dynamics by the end of 2024; but these predictions contradict some of the observed
214 pathogen dynamics. For example, we predict that both human metapneumovirus and
215 RSV in Korea should have returned to their attractors by now, but the magnitude
216 and timing of recent epidemics are different from pre-pandemic patterns (Figure 1).
217 These observations suggest the possibility that some common respiratory pathogens
218 may have converged to different attractors.

219 In Supplementary Materials, we also consider using a lower threshold for the false
220 nearest neighbor approach when determining the embedding dimension; this gives
221 a higher embedding dimension. As explained earlier (Supplementary Figure S6),

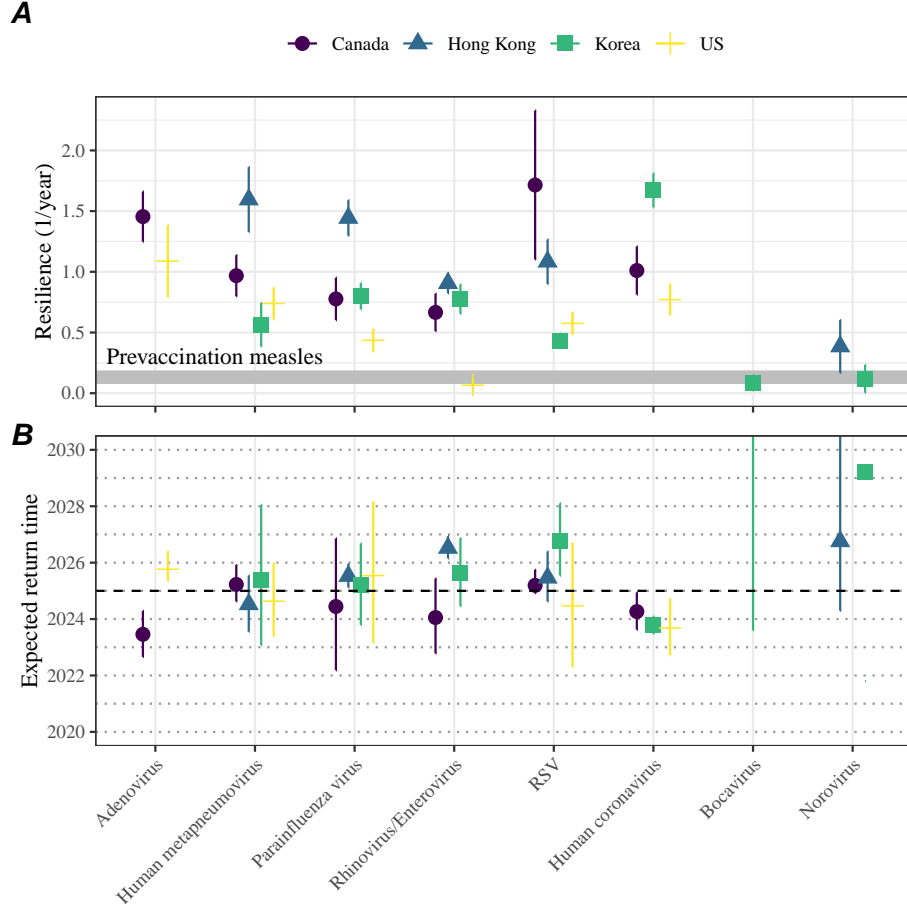


Figure 4: **Summary of resilience estimates.** (A) Estimated pathogen resilience. The gray horizontal line represents the intrinsic resilience of pre-vaccination measles dynamics. (B) Predicted timing of when each pathogen will return to their pre-pandemic cycles. The dashed line in panel B indicates the end of 2024 (current observation time). Error bars represent 95% confidence intervals.

this gives a smoother distance-from-attractor time series (compare Supplementary Figure S10 with S8); this also requires us to use longer time series, which prevents us from estimating resilience for some pathogens. Overall, resulting estimates of pathogen resilience with higher embedding dimensions still fall between 0.3/year and 2.1/year for the most part (Supplementary Figure S11). A direct comparison between two approaches (i.e., original estimate vs using higher dimensions) shows a strong consistency in resilience estimates (Supplementary Figure S12).

229 **Susceptible host dynamics explain variation in pathogen
230 resilience**

231 So far, we focused on quantifying pathogen resilience from the observed patterns of
 232 pathogen re-emergence following COVID-19 interventions. But what factors deter-
 233 mine how resilient a host-pathogen system is? Here, we use a standard Susceptible-
 234 Infected-Recovered-Susceptible (SIRS) model to show that susceptible host dynamics
 235 are the key determinants of pathogen resilience. To do so, we vary the basic reproduc-
 236 tion number \mathcal{R}_0 , which represents the average number of secondary infections caused
 237 by a newly infected individual in a fully susceptible population, and the duration of
 238 immunity and compute intrinsic resilience for each parameter.

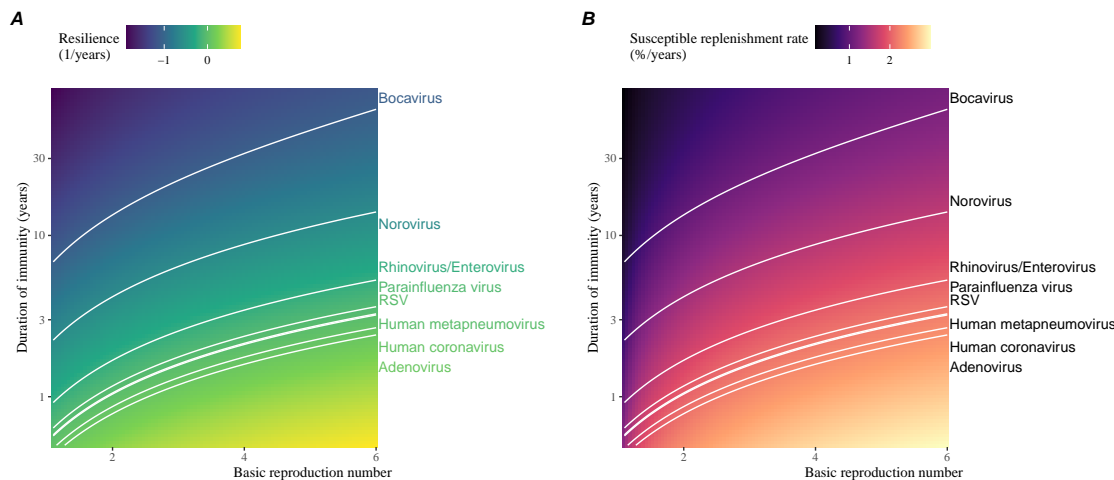


Figure 5: **Linking pathogen resilience to epidemiological parameters and susceptible host dynamics.** (A) The heat map represents intrinsic resilience as a function of the basic reproduction number \mathcal{R}_0 and the duration of immunity. (B) The heat map represents per-capita susceptible replenishment rate as a function of the basic reproduction number \mathcal{R}_0 and the duration of immunity. The standard SIRS model is used to compute intrinsic resilience and per-capita susceptible replenishment rate. Lines correspond to a set of parameters that are consistent with mean resilience estimates for each pathogen. Pathogens are ranked based on their mean resilience estimates, averaged across different countries.

239 We find an increase in \mathcal{R}_0 and a decrease in duration of immunity correspond
 240 to an increase in pathogen resilience (Figure 5A). These variations can be under-
 241 stood in terms of the susceptible host dynamics, where faster per-capita susceptible
 242 replenishment rate causes the system to be more resilient (Figure 5B). This rate can
 243 be expressed as a ratio between absolute rate at which new susceptibles enter the
 244 population and the equilibrium number of susceptible individuals in the population,
 245 \bar{S} . Therefore, both higher \mathcal{R}_0 and shorter duration of immunity can drive faster

246 per-capita susceptible replenishment rate (Figure 5B), especially because higher \mathcal{R}_0
247 leads to lower \bar{S} .

248 Finally, we can now rank different pathogens based on the average values of em-
249 pirical resilience, which allows us to determine a set of parameters that are consistent
250 with the estimated resilience (Figure 5A). Across all pathogens we consider, except
251 for bocavirus and norovirus, we estimate that the average duration of immunity is
252 likely to be short (< 6 years) across a plausible range of \mathcal{R}_0 . These rankings further
253 allow us to map each pathogen onto a set of parameters that are consistent with
254 its empirical resilience (Figure 5A) and obtain a plausible range of susceptible re-
255 plenishment rates for each pathogen (Figure 5B). However, we note that there is no
256 one-to-one correspondence between susceptible replenishment rates and pathogen re-
257 silience, leading to a wide uncertainty in the estimates for susceptible replenishment
258 rates (Figure 5B).

259 Discussion

260 The COVID-19 interventions have caused major disruptions to circulation patterns
261 of both respiratory and non-respiratory pathogens, adding challenges to predicting
262 their future dynamics [1, 2, 3, 4]. On the other hand, these interventions offer
263 large-scale natural experiments for understanding how different pathogens respond to
264 perturbations. In this study, we show that pathogen re-emergence patterns following
265 COVID-19 interventions can be characterized through the lens of ecological resilience.
266 Traditionally, ecological resilience measures how fast a system returns to a reference
267 state following a perturbation. In the context of respiratory pathogens, resilience
268 measures how fast epidemics return to their endemic cycles after interventions are
269 lifted.

270 We use an attractor reconstruction approach to quantify how distance from at-
271 tractor changes over time for each pathogen [14]. We show that the resilience of
272 a host-pathogen system can be estimated by fitting a linear regression to a logged
273 distance-from-attractor time series. Overall, we estimate that the resilience for most
274 common respiratory pathogens ranges between 0.4/year and 1.8/year, which is 3–14
275 times more resilient than prevaccination measles, indicating potential challenges in
276 controlling common respiratory pathogens.

277 Our framework allows us to make phenomenological predictions about when each
278 pathogen will return to their endemic cycles. The ability to predict future epidemic
279 patterns from resilience estimates offers a new paradigm for epidemic forecasting.
280 While this approach cannot predict the exact timing of outbreaks or epidemic pat-
281 terns, it is nonetheless useful for predicting when epidemics will settle down to regular
282 cycles after a large perturbation, such as COVID-19 interventions.

283 Our analyses suggest a possibility that several pathogens may have converged
284 to different endemic cycles compared to their pre-pandemic epidemic patterns. Key
285 examples include human metapnuemovirus, RSV, and bocavirus in Korea as well as

286 RSV in Hong Kong. These changes may reflect changes in surveillance or actual shift
287 in the dynamics, caused by permanent changes in behavior or population-level immu-
288 nity. While it seems unlikely that permanent changes in behavior would only affect a
289 few pathogens and not others, we cannot rule out this possibility given heterogeneity
290 in the age of infection across different respiratory pathogens [SWP: CITE]. A shift
291 in population-level immunity is plausible, as the emergence of SARS-CoV-2 and ex-
292 tinction of influenza B/Yamagata likely caused major changes in immune landscapes;
293 interactions among co-circulating pathogens, such as cross immunity between RSV
294 and HMPV [18], may have also contributed to changes in population-level immu-
295 nity. However, we currently do not know how immunity, or lack thereof, from these
296 pathogens would affect infection from other pathogens. Future studies should use
297 detailed mechanistic models, coupled with behavioral and immunological data, to
298 test these hypotheses and better understand post-pandemic dynamics of endemic
299 pathogens.

300 We show that susceptible host dynamics shape pathogen resilience, where faster
301 replenishment of the susceptible population causes the pathogen to be more resilient.
302 For simplicity, we focus on waning immunity and birth as a main driver of the suscep-
303 tible host dynamics but other mechanisms can also contribute to the replenishment
304 of the susceptible population. In particular, pathogen evolution, especially the emer-
305 gence of antigenically novel strains, can cause effective waning of immunity in the
306 population; therefore, we hypothesize that faster rates of antigenic evolution can also
307 cause a pathogen to be more resilient. Future studies should explore the relationship
308 between the rate of evolution and resilience for antigenically evolving pathogens.

309 Quantifying pathogen resilience also offers novel approaches to validating population-
310 level epidemiological models. So far, the majority of model validation in epidemiology
311 is based on the ability of a model to reproduce the observed epidemic dynamics and
312 to predict future dynamics [19, 18, 20, 21, 22]. However, there can be plethora of
313 models that meet these criteria. For example, two major RSV models have been pro-
314 posed so far to explain biennial epidemic patterns: (1) a stage- and age-structured
315 model that allows for disease severity to vary with number of past infections and
316 age of infection [20] and (2) a pathogen-interaction model that accounts for cross
317 immunity between RSV and human metapnuemovirus [18]. Since both models can
318 accurately reproduce the observed epidemic patterns, standard criteria for model
319 validation do not allow us to distinguish between these two models from population-
320 level data alone. Instead, we can measure the empirical resilience of each model
321 by simulating various perturbations and compare them to estimates of empirical re-
322 siliience from data, using COVID-19 interventions as an opportunity. Future studies
323 should further investigate using pathogen resilience for validating epidemic models.

324 There are several limitations to our work. First of all, we did not extensively ex-
325 plore other approaches to reconstructing the attractor. Recent studies showed that
326 more sophisticated approaches, such as using non-uniform embedding, can provide
327 more robust reconstruction for noisy data [17]. In the context of causal inference,
328 choices about embedding can have major impact on the resulting inference [23]. Our

resilience estimates are likely overly confident given a lack of uncertainties in attractor reconstruction as well as the simplicity of our statistical framework. Short pre-pandemic time series also contributes to the crudeness of our estimates. Nonetheless, as illustrated in our sensitivity analyses (Supplementary Figure S6, S10–S12), inferences about pathogen resilience appear to be robust to decisions about embedding lags and dimensions—this is because tracking the rate at which the system approaches the attractor is likely a much simpler problem than making inferences about causal directionality. Our qualitative prediction that common respiratory pathogens are more resilient than prevaccination measles is also likely to be robust to these predictions, given how rapid many respiratory pathogens returned to their original cycles following COVID-19 interventions.

Predicting the impact of anthropogenic changes on infectious disease dynamics is a fundamental aim of infectious disease research in a rapidly changing world. Our study illustrates that quantifying pathogen resilience can help us understand how infectious disease pathogens respond to major perturbations caused by public health interventions. More broadly, a detailed understanding of the determinants of pathogen resilience may offer unique insights into pathogen persistence and controllability.

Materials and Methods

Data

We gathered time series on respiratory infections from four different countries: Canada, Hong Kong, Korea, and United States (US). As a reference, we also included time series data on norovirus infections for available countries—in contrast to respiratory pathogens, we expect gastrointestinal viruses, such as norovirus, to be less affected by COVID-19 intervention measures. For all time series, we rounded every year to 52 weeks by taking the average number of cases and tests between the 52nd and 53rd week. We also rescale all time series to account for changes in testing patterns, which are then used for the actual analysis.

Weekly time series of respiratory infection cases in Canada comes from the Respiratory Virus Detection Surveillance System, which collect data from select laboratories across Canada. We extract the data from <https://www.canada.ca/en/public-health/services/surveillance/respiratory-virus-detections-canada.html>. To account for an increase in testing from 2013 to 2024, we calculate a 2 year moving average for the number of tests for each pathogen, which we use as a proxy for testing effort. Then, we divide the smoothed testing patterns by the smoothed value at the final week such that the testing effort has a maximum of 1. We then divide weekly cases by the testing effort to obtain a scaled case time series. A similar approach was used earlier for the analysis of RSV time series in the US [20].

Weekly time series of respiratory infection cases in Hong Kong comes from the Centre for Health Protection, Department of Health. We extract the data from

369 <https://www.chp.gov.hk/en/statistics/data/10/641/642/2274.html>. We also
370 apply the same scaling procedure to the time series as we did for Canada. For Hong
371 Kong, we only adjust for testing efforts up to the end of 2019 because there was a
372 major reduction in testing for common respiratory pathogens since 2020.

373 Weekly time series of acute respiratory infection cases in Korea comes from Ko-
374 rea Disease Control and Prevention Agency. We extract the data from <https://dportal.kdca.go.kr/pot/is/st/ari.do>. While we do not have information on
375 testing, the reported number of respiratory infections consistently increased from
376 2013 to the end of 2019, which we interpreted as changes in testing patterns. Since
377 we do not have testing numbers, we used the weekly sum of all acute respiratory vi-
378 ral infection cases as a proxy for testing, which were further smoothed with moving
379 averaged and scaled to have a maximum of 1. For Korea, we also only adjust for
380 testing efforts up to the end of 2019.

382 Finally, weekly time series of respiratory infection cases in the US comes from
383 the National Respiratory and Enteric Virus Surveillance System. In the US, there
384 has been a large increase in testing against some respiratory pathogens, especially
385 RSV, which could not be corrected for through simple scaling. Instead, we derive an
386 incidence proxy by multiplying the test positivity with influenza-like illness positivity,
387 which is taken from <https://gis.cdc.gov/grasp/fluvview/fluportaldashboard.html>. This method of estimating an incidence proxy has been recently applied in
388 the analysis of seasonal coronaviruses [7] and Mycoplasma pneumoniae infections [4].
389 Detailed assumptions and justifications are provided in [24].

391 Estimating pathogen resilience

392 In order to measure pathogen resilience from surveillance data, we first reconstruct
393 the empirical pre-pandemic attractor of the system using Takens' embedding theorem
394 [14]. Specifically, for a given pathogen, we take the pre-pandemic (before 2020)
395 case time series $C(t)$ and reconstruct the attractor using delayed embedding with a
396 uniform delay of τ and dimension M :

$$X_{\tau,m}(t) = \langle \log(C(t) + 1), \log(C(t - \tau) + 1), \dots, \log(C(t - (M - 1)\tau) + 1) \rangle. \quad (2)$$

397 Here, the delay τ is determined by looking at the autocorrelation of the logged pre-
398 pandemic time series and asking when the autocorrelation crosses 0 for the first time
399 [17]; a typical delay for an annual outbreak is around 13 weeks.

400 Then, for a given delay τ , we determine the embedding dimension M using the
401 false nearest neighbors approach [16, 17]. To do so, we start with an embedding
402 dimension e and construct a set of points $A_{\tau,e} = \{X_{\tau,e}(t) | t < 2020\}$. Then, for
403 each point $X_{\tau,e}(t)$, we determine the nearest neighbor from the set $A_{\tau,e}$, which we
404 denote $X_{\tau,e}(t_{nn})$ for $t \neq t_{nn}$. Then, if the distance between these two points on $e + 1$
405 dimension, $D_{\tau,e+1}(t) = \|X_{\tau,e+1}(t_{nn}) - X_{\tau,e+1}(t)\|_2$, is larger than their distance on
406 e dimension, $D_{\tau,e}(t) = \|X_{\tau,e}(t_{nn}) - X_{\tau,e}(t)\|_2$, these two points are deemed to be
407 false nearest neighbors; specifically, we use a threshold R for the ratio between two

408 distances $D_{\tau,e+1}(t)/D_{\tau,e}(t)$ to determine false nearest neighbors. In the main text,
 409 we determine embedding dimension based as the first dimension without any false
 410 nearest neighbors for $R = 10$. In Supplementary Materials, we impose $R = 5$ to select
 411 for higher dimensions. Once we determine the embedding lag τ and dimension M ,
 412 we apply the embedding to the entire time series and calculate the nearest neighbor
 413 distance against the attractor $A_{\tau,M}$ to obtain a time series of distance from attractor
 414 $D_{\tau,M}(t)$.

415 From a time series of distance from attractor, we estimate pathogen resilience
 416 by fitting a linear regression to an appropriate window. To automatically select
 417 the fitting window, we begin by smoothing the distance time series using locally
 418 estimated scatterplot smoothing (LOESS) to obtain $\hat{D}_{\tau,M}(t)$, where the smoothing
 419 is performed on a log scale and exponentiated afterwards. Then, we determine
 420 threshold values (T_{start} and T_{end}) for the smoothed distances and choose the fitting
 421 window based on when $\hat{D}_{\tau,M}(t)$ crosses these threshold values for the first time.
 422 These thresholds are determined by first calculating maximum distance,

$$\max \hat{D} = \max \hat{D}_{\tau,M}(t), \quad (3)$$

423 and mean pre-pandemic distance,

$$\hat{D}_{\text{mean}} = \frac{1}{N_{t < 2020}} \sum_{t < 2020} \hat{D}_{\tau,M}(t), \quad (4)$$

424 as a reference, and then dividing their ratios into 10 equal bins:

$$T_{\text{start}} = \hat{D}_{\text{mean}} \times \left(\frac{\max \hat{D}}{\hat{D}_{\text{mean}}} \right)^{9/10} \quad (5)$$

$$T_{\text{end}} = \hat{D}_{\text{mean}} \times \left(\frac{\max \hat{D}}{\hat{D}_{\text{mean}}} \right)^{1/10} \quad (6)$$

425 This allows us to discard the initial period during which the distance increases (from
 426 the introduction of intervention measures) and the final period during which the
 427 distance plateaus (as the system reaches an attractor). The fitting window is deter-
 428 mined based on when the smoothed distance $\hat{D}_{\tau,M}(t)$ crosses these threshold values
 429 for the first time; then, we fit a linear regression to logged (unsmoothed) distances
 430 $\log D_{\tau,M}(t)$ using that window.

431 Mathematical modeling

432 Throughout the paper, we use a series of mathematical models to illustrate the con-
 433 cept of pathogen resilience and to understand the determinants of pathogen resilience.
 434 In general, the intrinsic resilience for a given system is given by the largest real part
 435 of the eigenvalues of the linearized system at endemic equilibrium. Here, we focus on

436 the SIRS model and present the details of other models in Supplementary Materials.
 437 The SIRS (Susceptible-Infected-Recovered-Susceptible) model is the simplest model
 438 that allows for waning of immunity, where recovered (immune) individuals are as-
 439 sumed to become fully susceptible after an average of $1/\delta$ time period. The dynamics
 440 of the SIRS model is described by the following set of differential equations:

$$\frac{dS}{dt} = \mu - \beta(t)SI - \mu S + \delta R \quad (7)$$

$$\frac{dI}{dt} = \beta(t)SI - (\gamma + \mu)I \quad (8)$$

$$\frac{dR}{dt} = \gamma I - (\delta + \mu)R \quad (9)$$

(10)

441 where μ represents the birth/death rate, $\beta(t)$ represents the time-varying trans-
 442 mission rate, and γ represents the recovery rate. The basic reproduction number
 443 $\mathcal{R}_0 = \beta(t)/(\gamma + \mu)$ is defined as the average number of secondary infections caused
 444 by a single infected individual in a fully susceptible population and measures the
 445 intrinsic transmissibility of a pathogen.

446 When we first introduce the idea of pathogen resilience (Figure 2), we impose
 447 sinusoidal changes to the transmission rate to account for seasonal transmission:

$$\beta(t) = b_1(1 + \theta \cos(2\pi(t - \phi)))\alpha(t), \quad (11)$$

448 where b_1 represents the baseline transmission rate, θ represents the seasonal ampli-
 449 tude, and ϕ represents the seasonal offset term. Here, we also introduce an extra
 450 multiplicative term $\alpha(t)$ to account for the impact of COVID-19 interventions, where
 451 $\alpha(t) < 1$ indicates transmission reduction. Figure 2A and 2B are generated assuming
 452 $b_1 = 3 \times (365/7 + 1/50)/\text{years}$, $\theta = 0.2$, $\phi = 0$, $\mu = 1/50/\text{years}$, $\gamma = 365/7/\text{years}$, and
 453 $\delta = 1/2/\text{years}$. In Figure 2A, we impose a 50% transmission reduction for 6 months
 454 from 2020:

$$\alpha(t) = \begin{cases} 0.5 & 2020 \leq t < 2020.5 \\ 1 & \text{otherwise} \end{cases} \quad (12)$$

455 In Figure 2B, we impose a 50% transmission reduction for 6 months from 2020 and
 456 a permanent 10% reduction onward:

$$\alpha(t) = \begin{cases} 1 & t < 2020 \\ 0.5 & 2020 \leq t < 2020.5 \\ 0.9 & 2020.5 \leq t \end{cases} \quad (13)$$

457 In both scenarios, we simulate the SIRS model from the following initial conditions
 458 ($S(0) = 1/\mathcal{R}_0$, $I(0) = 1 \times 10^{-6}$, and $R(0) = 1 - S(0) - I(0)$) from 1900 until 2030.

459 To measure the empirical resilience of the SIR model (Figure 2C and 2F), we
 460 compute the normalized distance between post-intervention susceptible and logged

⁴⁶¹ infected proportions and their corresponding pre-intervention values at the same time
⁴⁶² of year:

$$\sqrt{\left(\frac{S(t) - S_{\text{pre}}(t)}{\sigma_S}\right)^2 + \left(\frac{\log I(t) - \log I_{\text{pre}}(t)}{\sigma_{\log I}}\right)^2}, \quad (14)$$

⁴⁶³ where σ_S and $\sigma_{\log I}$ represent the standard deviation in the pre-intervention suscep-
⁴⁶⁴ tible and logged infected proportions. We normalize the differences in susceptible
⁴⁶⁵ and logged infected proportions to allow both quantities to equally contribute to the
⁴⁶⁶ changes in distance from attractor. In Supplementary Materials, we also compare
⁴⁶⁷ the how the degree of seasonal transmission affects empirical resilience by varying
⁴⁶⁸ θ from 0 to 0.4; when we assume no seasonality ($\theta = 0$), we do not normalize the
⁴⁶⁹ distance because the standard deviation of pre-intervention dynamics are zero.

⁴⁷⁰ Finally, we use the SIRS model to understand how underlying epidemiological
⁴⁷¹ parameters affect pathogen resilience and link this relationship to underlying sus-
⁴⁷² ceptible host dynamics. For the simple SIRS model without seasonal transmission
⁴⁷³ ($\theta = 0$), the intrinsic resilience corresponds to:

$$-\frac{\text{Re}(\lambda)}{2} = \frac{\delta + \beta I^* + \mu}{2}. \quad (15)$$

⁴⁷⁴ Here, I^* represents the prevalence values at endemic equilibrium:

$$I^* = \frac{(\delta + \mu)(\beta - (\gamma + \mu))}{\beta(\delta + \gamma + \mu)}. \quad (16)$$

⁴⁷⁵ The susceptible replenishment rate is given by:

$$S_{\text{replenish}} = \frac{\mu + \delta R}{S^*}, \quad (17)$$

⁴⁷⁶ where $S^* = 1/\mathcal{R}_0$ represents the equilibrium proportion of susceptible individuals.
⁴⁷⁷ We vary the basic reproduction number \mathcal{R}_0 between 1.1 to 6 and the average duration
⁴⁷⁸ of immunity $1/\delta$ between 2 to 80 years, and compute these two quantities. In doing
⁴⁷⁹ so, we fix all other parameters: $\mu = 1/80/\text{years}$ and $\gamma = 365/7/\text{years}$.

480 **Supplementary Text**

481 **Resilience of a stage-structured system.**

482 In Figure 2G–I, we use a more realistic, stage-structured model to illustrate how
 483 transient phenomena can cause the system to slow down. Specifically, we use the
 484 stage-structured RSV model proposed by [20], which assumes that subsequent rein-
 485 fections cause an individual to become less susceptible and transmissible than previ-
 486 ous infections. The model dynamics can be described as follows:

$$\frac{dM}{dt} = \mu - (\omega + \mu)M \quad (S1)$$

$$\frac{dS_0}{dt} = \omega M - (\lambda(t) + \mu)S_0 \quad (S2)$$

$$\frac{dI_1}{dt} = \lambda(t)S_0 - (\gamma_1 + \mu)I_1 \quad (S3)$$

$$\frac{dS_1}{dt} = \gamma_1 I_1 - (\sigma_1 \lambda(t) + \mu)S_1 \quad (S4)$$

$$\frac{dI_2}{dt} = \sigma_1 \lambda(t)S_1 - (\gamma_2 + \mu)I_2 \quad (S5)$$

$$\frac{dS_2}{dt} = \gamma_2 I_2 - (\sigma_2 \lambda(t) + \mu)S_2 \quad (S6)$$

$$\frac{dI_3}{dt} = \sigma_2 \lambda(t)S_2 - (\gamma_3 + \mu)I_3 \quad (S7)$$

$$\frac{dS_3}{dt} = \gamma_3 I_3 - (\sigma_3 \lambda(t) + \mu)S_3 + \gamma_4 I_4 \quad (S8)$$

$$\frac{dI_4}{dt} = \sigma_3 \lambda(t)S_3 - (\gamma_4 + \mu)I_4 \quad (S9)$$

(S10)

487 where M represents the proportion of individuals who are maternally immune; S_i
 488 represents the proportion of individuals who are susceptible after i prior infections; I_i
 489 represents the proportion of individuals who are currently (re)-infected with their i -th
 490 infection; μ represents the birth and death rates; $1/\omega$ represents the mean duration
 491 of maternal immunity; $1/\gamma_i$ represents the mean duration of infection; $\lambda(t)$ represents
 492 the force of infection; and σ_i represents the reduction in susceptibility for reinfection.
 493 The force of infection is modeled using a sinusoidal function:

$$\beta(t) = b_1(1 + \theta \cos(2\pi(t - \phi)))\alpha(t) \quad (S11)$$

$$\lambda(t) = \beta(I_1 + \rho_1 I_2 + \rho_2(I_3 + I_4)), \quad (S12)$$

494 where b_1 represents the baseline transmission rate; θ represents the seasonal ampli-
 495 tude; ϕ represents the seasonal offset term; $\alpha(t)$ represents the intervention effect;
 496 and ρ_i represents the impact of immunity on transmission reduction. We use the

497 following parameters to simulate the impact of interventions on epidemic dynam-
 498 ics [20]: $b_1 = 9 \times (365/10 + 1/80)/\text{years}$, $\theta = 0.2$, $\phi = -0.1$, $\omega = 365/112/\text{years}$,
 499 $\gamma_1 = 365/10/\text{years}$, $\gamma_2 = 365/7/\text{years}$, $\gamma_3 = 365/5/\text{years}$, $\sigma_1 = 0.76$, $\sigma_2 = 0.6$,
 500 $\sigma_3 = 0.4$, $\rho_1 = 0.75$, $\rho_2 = 0.51$, and $\mu = 1/80/\text{years}$. We assume a 50% transmission
 501 reduction for 6 months from 2020:

$$\alpha(t) = \begin{cases} 0.5 & 2020 \leq t < 2020.5 \\ 1 & \text{otherwise} \end{cases} \quad (\text{S13})$$

502 The model is simulated from 1900 to 2030 using the following initial conditions:
 503 $M = 0$, $S_0 = 1/\mathcal{R}_0 - I_1$, $I_1 = 1 \times 10^{-6}$, $S_1 = 1 - 1/\mathcal{R}_0$, $I_2 = 0$, $S_2 = 0$, $I_3 = 0$,
 504 $S_3 = 0$, and $I_4 = 0$. For the phase plane analysis (Figure 2H) and distance analysis
 505 (Figure 2I), we rely on the average susceptibility,

$$\bar{S} = S_0 + \sigma_1 S_1 + \sigma_2 S_2 + \sigma_3 S_3, \quad (\text{S14})$$

506 and total prevalence,

$$I_{\text{total}} = I_1 + I_2 + I_3 + I_4. \quad (\text{S15})$$

507 These quantities are used to compute the normalized distance from the attractor, as
 508 described in the main text.

509 Resilience of a multistrain system.

510 We use a simple two-strain model to show that a multistrain host-pathogen system
 511 that is coupled through cross immunity can be described by a single resilience value.
 512 The model dynamics can be described as follows [18]:

$$\frac{dS}{dt} = \mu - \mu S - (\lambda_1 + \lambda_2)S + \rho_1 R_1 + \rho_2 R_2 \quad (\text{S16})$$

$$\frac{dI_1}{dt} = \lambda_1 S - (\gamma_1 + \mu)I_1 \quad (\text{S17})$$

$$\frac{dI_2}{dt} = \lambda_2 S - (\gamma_2 + \mu)I_2 \quad (\text{S18})$$

$$\frac{dR_1}{dt} = \gamma_1 I_1 - \lambda_2 \epsilon_{21} R_1 - \rho_1 R_1 + \rho_2 R - \mu R_1 \quad (\text{S19})$$

$$\frac{dR_2}{dt} = \gamma_2 I_2 - \lambda_1 \epsilon_{12} R_2 - \rho_2 R_2 + \rho_1 R - \mu R_2 \quad (\text{S20})$$

$$\frac{dJ_1}{dt} = \lambda_1 \epsilon_{12} R_2 - (\gamma_1 + \mu) J_1 \quad (\text{S21})$$

$$\frac{dJ_2}{dt} = \lambda_2 \epsilon_{21} R_1 - (\gamma_2 + \mu) J_2 \quad (\text{S22})$$

$$\frac{dR}{dt} = \gamma_1 J_1 + \gamma_2 J_2 - \rho_1 R - \rho_2 R - \mu R \quad (\text{S23})$$

513 where S represents the proportion of individuals who are fully susceptible to infections
 514 by both strains; I_1 represents the proportion of individuals who are infected with strain 1 without prior immunity; I_2 represents the proportion of individuals who are infected with strain 2 without prior immunity; R_1 represents the proportion of individuals who are fully immune against strain 1 and partially susceptible to reinfection by strain 2; R_2 represents the proportion of individuals who are fully immune against strain 2 and partially susceptible to reinfection by strain 1; J_1 represents the proportion of individuals who are infected with strain 1 with prior immunity against strain 2; J_2 represents the proportion of individuals who are infected with strain 2 with prior immunity against strain 1; R represents the proportion of individuals who are immune to infections from both strains; μ represents the birth/death rate; λ_1 and λ_2 represent the force of infection from strains 1 and 2, respectively; ρ_1 and ρ_2 represent the waning immunity rate; γ_1 and γ_2 represent the recovery rate; ϵ_{12} and ϵ_{21} represent the susceptibility to reinfection with strains 2 and 1, respectively, given prior immunity from infection with strains 1 and 2, respectively. The force of infection is modeled as follows:

$$\beta_1 = b_1(1 + \theta_1 \sin(2\pi(t - \phi_1)))\alpha(t) \quad (\text{S24})$$

$$\beta_2 = b_2(1 + \theta_2 \sin(2\pi(t - \phi_2)))\alpha(t) \quad (\text{S25})$$

$$\lambda_1 = \beta_1(I_1 + J_1) \quad (\text{S26})$$

$$\lambda_2 = \beta_2(I_2 + J_2) \quad (\text{S27})$$

529 In Supplementary Figures S2–S4, we assume the following parameters: $b_1 = 2 \times$
 530 $52/\text{years}$, $b_2 = 4 \times 52/\text{years}$, $\phi_1 = \phi_2 = 0$, $\epsilon_{12} = 0.9$, $\epsilon_{21} = 0.5$, $\gamma_1 = \gamma_2 = 52/\text{years}$,
 531 $\rho_1 = \rho_2 = 1/\text{years}$, and $\mu = 1/70/\text{years}$. For all simulations, we assume a 50%
 532 transmission reduction for 6 months from 2020:

$$\alpha(t) = \begin{cases} 0.5 & 2020 \leq t < 2020.5 \\ 1 & \text{otherwise} \end{cases} \quad (\text{S28})$$

533 The seasonal amplitude θ is varied from 0 to 0.4. All simulations are ran from 1900
 534 to 2030 from the following initial conditions: $S(0) = 1 - 2 \times 10^{-6}$, $I_1(0) = 1 \times 10^{-6}$,
 535 $I_2(0) = 1 \times 10^{-6}$, $R_1(0) = 0$, $R_2(0) = 0$, $J_1(0) = 0$, $J_2(0) = 0$, and $R(0) = 0$.

536 For this, we consider three different scenarios for measuring pathogen resilience:
 537 (1) we only have information about strain 1, (2) we only have information about
 538 strain 2, and (3) we are unable to distinguish the differences between strains. In
 539 the first two scenarios (see panels A–C for strain 1 and panels D–F for strain 2), we
 540 consider the dynamics of average susceptibility for each strain and total prevalence:

$$\bar{S}_1 = S + \epsilon_{12}R_2 \quad (\text{S29})$$

$$\hat{I}_1 = I_1 + J_1 \quad (\text{S30})$$

$$\bar{S}_2 = S + \epsilon_{21}R_1 \quad (\text{S31})$$

$$\hat{I}_2 = I_2 + J_2 \quad (\text{S32})$$

⁵⁴¹ In the third scenario (panels G–I), we consider the dynamics of total susceptible and
⁵⁴² infected population:

$$\hat{S} = S + R_2 + R_1 \quad (\text{S33})$$

$$\hat{I} = I_1 + J_1 + I_2 + J_2 \quad (\text{S34})$$

$$(\text{S35})$$

⁵⁴³ These quantities are used to compute the normalized distance from the attractor, as
⁵⁴⁴ described in the main text.

⁵⁴⁵ Estimating intrinsic resilience using mechanistic model

⁵⁴⁶ We test whether we can reliably estimate the intrinsic resilience of a system by fitting
⁵⁴⁷ a mechanistic model. Specifically, we simulate case time series from stochastic SIRS
⁵⁴⁸ and two-strain models and fit a simple, deterministic SIRS model using a Bayesian
⁵⁴⁹ framework.

⁵⁵⁰ First, we describe the simulation set up. The stochastic SIRS model can be
⁵⁵¹ written as follows:

$$\beta(t) = \mathcal{R}_0 \left(1 + \theta \cos \left(\frac{2\pi t}{364} \right) \right) \alpha(t)(1 - \exp(-\gamma)) \quad (\text{S36})$$

$$\text{FOI}(t) = \beta(t)I(t - \Delta t)/N \quad (\text{S37})$$

$$B(t) \sim \text{Poisson}(\mu N) \quad (\text{S38})$$

$$\Delta S(t) \sim \text{Binom}(S(t - \Delta t), 1 - \exp(-(\text{FOI}(t) + \mu)\Delta t)) \quad (\text{S39})$$

$$N_{SI}(t) \sim \text{Binom}\left(\Delta S(t), \frac{\text{FOI}(t)}{\text{FOI}(t) + \mu}\right) \quad (\text{S40})$$

$$\Delta I(t) \sim \text{Binom}(I(t - \Delta t), 1 - \exp(-(\gamma + \mu)\Delta t)) \quad (\text{S41})$$

$$N_{IR}(t) \sim \text{Binom}\left(\Delta I(t), \frac{\gamma}{\gamma + \mu}\right) \quad (\text{S42})$$

$$\Delta R(t) \sim \text{Binom}(R(t - \Delta t), 1 - \exp(-(\delta + \mu)\Delta t)) \quad (\text{S43})$$

$$N_{RS}(t) \sim \text{Binom}\left(\Delta R(t), \frac{\delta}{\delta + \mu}\right) \quad (\text{S44})$$

$$S(t) = S(t - \Delta t) + N_{RS}(t) + B(t) - \Delta S(t) \quad (\text{S45})$$

$$I(t) = I(t - \Delta t) + N_{SI}(t) - \Delta I(t) \quad (\text{S46})$$

$$R(t) = R(t - \Delta t) + N_{IR}(t) - \Delta R(t) \quad (\text{S47})$$

⁵⁵² where FOI represent the force of infection; N_{ij} represent the number of individuals
⁵⁵³ moving from compartment i to j on a given day; and $B(t)$ represents the number
⁵⁵⁴ of new births. We simulate the model on a daily scale—assuming 364 days in a
⁵⁵⁵ year so that it can be evenly grouped into 52 weeks—with the following parameters:
⁵⁵⁶ $\mathcal{R}_0 = 3$, $\theta = 0.1$, $\gamma = 1/7/\text{days}$, $\delta = 1/(364 \times 2)/\text{days}$, $\mu = 1/(364 \times 50)/\text{days}$, and

⁵⁵⁷ $N = 1 \times 10^8$. The model is simulated from 1900 to 2030 assuming $S(0) = N/3$,
⁵⁵⁸ $I(0) = 100$, and $R(0) = N - S(0) - I(0)$. The observed incidence from the model is
⁵⁵⁹ then simulated as follows:

$$C(t) = \text{Beta} - \text{Binom}(N_{SI}(t), \rho, k), \quad (\text{S48})$$

⁵⁶⁰ where ρ represents the reporting probability and k represents the overdispersion pa-
⁵⁶¹ rameter of beta-binomial distribution. We assume $\rho = 0.002$ (i.e., 0.2% probability)
⁵⁶² and $k = 1000$.

⁵⁶³ The stochastic two-strain model can be written as follows:

$$\beta_1(t) = b_1 \left(1 + \theta_1 \cos \left(\frac{2\pi(t - \phi_1)}{364} \right) \right) \alpha(t) \quad (\text{S49})$$

$$\beta_2(t) = b_2 \left(1 + \theta_2 \cos \left(\frac{2\pi(t - \phi_2)}{364} \right) \right) \alpha(t) \quad (\text{S50})$$

$$\text{FOI}_1(t) = \beta_1(t)(I_1(t - \Delta t) + J_1(t - \Delta t))/N \quad (\text{S51})$$

$$\text{FOI}_2(t) = \beta_2(t)(I_2(t - \Delta t) + J_2(t - \Delta t))/N \quad (\text{S52})$$

$$B(t) \sim \text{Poisson}(\mu N) \quad (\text{S53})$$

$$\Delta S(t) \sim \text{Binom}(S(t - \Delta t), 1 - \exp(-(\text{FOI}_1(t) + \text{FOI}_2(t) + \mu)\Delta t)) \quad (\text{S54})$$

$$N_{SI_1}(t) \sim \text{Binom}\left(\Delta S(t), \frac{\text{FOI}_1(t)}{\text{FOI}_1(t) + \text{FOI}_2(t) + \mu}\right) \quad (\text{S55})$$

$$N_{SI_2}(t) \sim \text{Binom}\left(\Delta S(t), \frac{\text{FOI}_2(t)}{\text{FOI}_1(t) + \text{FOI}_2(t) + \mu}\right) \quad (\text{S56})$$

$$\Delta I_1(t) \sim \text{Binom}(I_1(t - \Delta t), 1 - \exp(-(\gamma_1 + \mu)\Delta t)) \quad (\text{S57})$$

$$N_{I_1 R_1}(t) \sim \text{Binom}\left(\Delta I_1(t), \frac{\gamma_1}{\gamma_1 + \mu}\right) \quad (\text{S58})$$

$$\Delta I_2(t) \sim \text{Binom}(I_2(t - \Delta t), 1 - \exp(-(\gamma_2 + \mu)\Delta t)) \quad (\text{S59})$$

$$N_{I_2 R_2}(t) \sim \text{Binom}\left(\Delta I_2(t), \frac{\gamma_2}{\gamma_2 + \mu}\right) \quad (\text{S60})$$

$$\Delta R_1(t) \sim \text{Binom}(R_1(t - \Delta t), 1 - \exp(-(\epsilon_{21}\text{FOI}_2(t) + \rho_1 + \mu)\Delta t)) \quad (\text{S61})$$

$$N_{R_1 S}(t) \sim \text{Binom}\left(\Delta R_1(t), \frac{\rho_1}{\epsilon_{21}\text{FOI}_2(t) + \rho_1 + \mu}\right) \quad (\text{S62})$$

$$N_{R_1 J_2}(t) \sim \text{Binom}\left(\Delta R_1(t), \frac{\epsilon_{21}\text{FOI}_2(t)}{\epsilon_{21}\text{FOI}_2(t) + \rho_1 + \mu}\right) \quad (\text{S63})$$

$$\Delta R_2(t) \sim \text{Binom}(R_2(t - \Delta t), 1 - \exp(-(\epsilon_{12}\text{FOI}_1(t) + \rho_2 + \mu)\Delta t)) \quad (\text{S64})$$

$$N_{R_2 S}(t) \sim \text{Binom}\left(\Delta R_2(t), \frac{\rho_2}{\epsilon_{12}\text{FOI}_1(t) + \rho_2 + \mu}\right) \quad (\text{S65})$$

$$N_{R_2 J_1}(t) \sim \text{Binom}\left(\Delta R_2(t), \frac{\epsilon_{12}\text{FOI}_1(t)}{\epsilon_{12}\text{FOI}_1(t) + \rho_2 + \mu}\right) \quad (\text{S66})$$

$$\Delta J_1(t) \sim \text{Binom}(J_1(t - \Delta t), 1 - \exp(-(\gamma_1 + \mu)\Delta t)) \quad (\text{S67})$$

$$N_{J_1R}(t) \sim \text{Binom}\left(\Delta J_1(t), \frac{\gamma_1}{\gamma_1 + \mu}\right) \quad (\text{S68})$$

$$\Delta J_2(t) \sim \text{Binom}(J_2(t - \Delta t), 1 - \exp(-(\gamma_2 + \mu)\Delta t)) \quad (\text{S69})$$

$$N_{J_2R}(t) \sim \text{Binom}\left(\Delta J_2(t), \frac{\gamma_2}{\gamma_2 + \mu}\right) \quad (\text{S70})$$

$$\Delta R(t) \sim \text{Binom}(R(t - \Delta t), 1 - \exp(-(\rho_1 + \rho_2 + \mu)\Delta t)) \quad (\text{S71})$$

$$N_{RR_1}(t) \sim \text{Binom}\left(\Delta R(t), \frac{\rho_1}{\rho_1 + \rho_2 + \mu}\right) \quad (\text{S72})$$

$$N_{RR_2}(t) \sim \text{Binom}\left(\Delta R(t), \frac{\rho_2}{\rho_1 + \rho_2 + \mu}\right) \quad (\text{S73})$$

$$S(t) = S(t - \Delta t) - \Delta S(t) + B(t) + N_{R_1S}(t) + N_{R_2S}(t) \quad (\text{S74})$$

$$I_1(t) = I_1(t - \Delta t) - \Delta I_1(t) + N_{SI_1}(t) \quad (\text{S75})$$

$$I_2(t) = I_2(t - \Delta t) - \Delta I_2(t) + N_{SI_2}(t) \quad (\text{S76})$$

$$R_1(t) = R_1(t - \Delta t) - \Delta R_1(t) + N_{I_1R_1}(t) + N_{RR_1}(t) \quad (\text{S77})$$

$$R_2(t) = R_2(t - \Delta t) - \Delta R_2(t) + N_{I_2R_2}(t) + N_{RR_2}(t) \quad (\text{S78})$$

$$J_1(t) = J_1(t - \Delta t) - \Delta J_1(t) + N_{R_2J_1}(t) \quad (\text{S79})$$

$$J_2(t) = J_2(t - \Delta t) - \Delta J_2(t) + N_{R_1J_2}(t) \quad (\text{S80})$$

$$R(t) = R(t - \Delta t) - \Delta R(t) + N_{J_1R}(t) + N_{J_2R}(t) \quad (\text{S81})$$

564 We simulate the model on a daily scale with previously estimated parameters for the
 565 RSV-HMPV interaction [18]: $b_1 = 1.7/\text{weeks}$, $b_2 = 1.95/\text{weeks}$, $\theta_1 = 0.4$, $\theta_2 = 0.3$,
 566 $\phi_1 = 0.005 \times 7/364$, $\phi_2 = 4.99 \times 7/364$, $\epsilon_{12} = 0.92$, $\epsilon_{21} = 0.45$, $\gamma_1 = 1/10/\text{days}$,
 567 $\gamma_2 = 1/10/\text{days}$, $\rho_1 = 1/364/\text{days}$, $\rho_2 = 1/364/\text{days}$, $\mu = 1/(70 \times 364)/\text{days}$, and
 568 $N = 1 \times 10^8$. The model is simulated from 1900 to 2030 assuming $S(0) = N - 200$,
 569 $I_1(0) = 100$, $I_2(0) = 100$, $R_1(0) = 0$, $R_2(0) = 0$, $J_1(0) = 0$, $J_2(0) = 0$, and $R(0) = 0$.
 570 The observed incidence for each strain is then simulated as follows:

$$C_1(t) = \text{Beta} - \text{Binom}(N_{SI_1}(t) + N_{R_2J_1}, \rho, k), \quad (\text{S82})$$

$$C_2(t) = \text{Beta} - \text{Binom}(N_{SI_2}(t) + N_{R_1J_2}, \rho, k), \quad (\text{S83})$$

571 where ρ represents the reporting probability and k represents the overdispersion pa-
 572 rameter of beta-binomial distribution. We assume $\rho = 0.002$ (i.e., 0.2% probability)
 573 and $k = 500$. We also consider the total incidence: $C_{\text{total}}(t) = C_1(t) + C_2(t)$.

574 For both models, we consider a more realistic challenges in intervention effects
 575 $\alpha(t)$ to challenge our ability to estimate the intervention effects. Thus, we assume
 576 a 40% transmission reduction for 3 months from March 2020, followed by a 10%
 577 transmission reduction for 6 months, 20% transmission reduction for 3 months, and

578 a final return to normal levels:

$$\alpha(t) = \begin{cases} 1 & t < 2020.25 \\ 0.6 & 2020.25 \leq t < 2020.5 \\ 0.9 & 2020.5 \leq t < 2021 \\ 0.8 & 2021 \leq t < 2021.25 \\ 1 & 2021.25 \leq t \end{cases}. \quad (\text{S84})$$

579 For all simulations, we truncate the time series from the beginning of 2014 to the
580 end of 2023 and aggregate them into weekly cases.

581 To infer intrinsic resilience from time series, we fit a simple discrete time, deter-
582 ministic SIRS model [4]:

$$\Delta t = 1 \text{ week} \quad (\text{S85})$$

$$\text{FOI}(t) = \beta(t)(I(t - \Delta t) + \omega)/N \quad (\text{S86})$$

$$\Delta S(t) = [1 - \exp(-(\text{FOI}(t) + \mu)\Delta t)] S(t - \Delta t) \quad (\text{S87})$$

$$N_{SI}(t) = \frac{\text{FOI}(t)\Delta S(t)}{\text{FOI}(t) + \mu} \quad (\text{S88})$$

$$\Delta I(t) = [1 - \exp(-(\gamma + \mu)\Delta t)] I(t - \Delta t) \quad (\text{S89})$$

$$N_{IR}(t) = \frac{\gamma \Delta I(t)}{\gamma + \mu} \quad (\text{S90})$$

$$\Delta R(t) = [1 - \exp(-(\nu + \mu)\Delta t)] R(t - \Delta t) \quad (\text{S91})$$

$$N_{RS}(t) = \frac{\nu \Delta R(t)}{\nu + \mu} \quad (\text{S92})$$

$$S(t) = S(t - \Delta t) + \mu S - \Delta S(t) + N_{RS}(t) \quad (\text{S93})$$

$$I(t) = I(t - \Delta t) - \Delta I(t) + N_{SI}(t) \quad (\text{S94})$$

$$R(t) = R(t - \Delta t) - \Delta R(t) + N_{IR}(t) \quad (\text{S95})$$

583 where we include an extra term ω to account for external infections. Although actual
584 simulations do not include any external infections, we found that including this term
585 generally helped with model convergence in previous analyses [4]. The transmission
586 rate is divided into a seasonal term $\beta_{\text{seas}}(t)$ (repeated every year) and intervention
587 term $\alpha(t)$, which are estimated jointly:

$$\beta(t) = \beta_{\text{seas}}(t)\alpha(t), \quad (\text{S96})$$

588 where $\alpha < 1$ corresponds to reduction in transmission due to intervention effects. To
589 constrain the smoothness of $\beta_{\text{seas}}(t)$, we impose cyclic, random-walk priors:

$$\beta_{\text{seas}}(t) \sim \text{Normal}(\beta_{\text{seas}}(t - 1), \sigma) \quad t = 2 \dots 52 \quad (\text{S97})$$

$$\beta_{\text{seas}}(1) \sim \text{Normal}(\beta_{\text{seas}}(52), \sigma) \quad (\text{S98})$$

590 [SWP: I noticed that I forgot to put a prior on σ so need to re-do this but won't
 591 change the results.] We fix $\alpha(t) = 1$ for all $t < 2020$ and estimate α assuming a
 592 normal prior:

$$\alpha \sim \text{Normal}(1, 0.25). \quad (\text{S99})$$

593 We assume weakly informative priors on ω and τ :

$$\omega \sim \text{Normal}(0, 200) \tau \sim \text{Normal}(104, 26) \quad (\text{S100})$$

594 We assume that the true birth/death rates, population sizes, and recovery rates are
 595 known. We note, however, that assuming $\gamma = 1/\text{week}$ actually correspond to a
 596 mean infectious period of 1.6 weeks, which is much longer than the true value; this
 597 approximation allows us to test whether we can still robustly estimate the intrinsic
 598 resilience given parameters mis-specification. Initial conditions are estimated with
 599 following priors:

$$S(0) = Ns(0) \quad (\text{S101})$$

$$I(0) = Ni(0) \quad (\text{S102})$$

$$s(0) \sim \text{Uniform}(0, 1) \quad (\text{S103})$$

$$i(0) \sim \text{Half-Normal}(0, 0.001) \quad (\text{S104})$$

600 Finally, the Observation model is specified as follows:

$$\text{Cases}(t) \sim \text{Negative-Binomial}(\rho N_{SI}(t), \phi) \quad (\text{S105})$$

$$\rho \sim \text{Half-Normal}(0, 0.02) \quad (\text{S106})$$

$$\phi \sim \text{Half-Normal}(0, 10) \quad (\text{S107})$$

601 where ρ represents the reporting probability and ϕ represents the negative binomial
 602 overdispersion parameter.

603 The model is fitted to four separate time series: (1) incidence time series from
 604 the SIRS model, (2) incidence time series for strain 1 from the two-strain model,
 605 (3) incidence time series for strain 2 from the two-strain model, and (4) combined
 606 incidence time series for strains 1 and 2 from the two-strain model. The model was
 607 fitted using rstan [25, 26]. The resulting posterior distribution was used to calculate
 608 the intrinsic resilience of the seasonally unforced system with the same parameters;
 609 eigenvalues of the discrete-time SIR model were computed by numerically finding
 610 the equilibrium and calculating the Jacobian matrix.

611 **Validations for window-selection criteria**

612 We use stochastic SIRS simulations to validate the window-selection criteria that we
 613 use for the linear regression for estimating empirical resilience. For each simulation,
 614 we begin by generating a random intervention $\alpha(t)$ from random set of parameters.
 615 First, we draw the duration of intervention τ_{np}^* from a uniform distribution between

616 0.5 and 3.5 years. Then, we draw independent normal variables z_i of length $\lfloor 364\tau_{\text{npi}} \rfloor$
 617 with a standard deviation of 0.02 and take a reverse cumulative sum to obtain a
 618 realistic shape for the intervention:

$$x_n = 1 + \sum_{i=n}^{\lfloor 364\tau_{\text{npi}} \rfloor} z_i, \quad n = 1, \dots, \lfloor 364\tau_{\text{npi}} \rfloor. \quad (\text{S108})$$

619 We repeat this random generation process until less than 10% of x_n exceeds 1. Then,
 620 we set any values that are above 1 or below 0 as 1 and 0, respectively. Then, we
 621 randomly draw the minimum transmission during intervention α_{\min} from a uniform
 622 distribution between 0.5 and 0.7 and scale x_n to have a minimum of α_{\min} :

$$x_{\text{scale},n} = \alpha_{\min} + (1 - \alpha_{\min}) \times \frac{x_n - \min x_n}{1 - \min x_n}. \quad (\text{S109})$$

623 This allows us to simulate a realistically shaped interventions:

$$\alpha(t) = \begin{cases} 1 & t < 2020 \\ x_{\text{scale},364(t-2020)} & 2020 \leq t < 2020 + \tau_{\text{npi}} \\ 1 & \tau_{\text{npi}} \leq t \end{cases}. \quad (\text{S110})$$

624 Given this intervention function, we draw \mathcal{R}_0 from a uniform distribution between 1.5
 625 and 3 and the mean duration of immunity $1/\delta$ from a uniform distribution between
 626 0.5 and 2. Then, we simulate the stochastic SIRS model from $S(0) = 10^8/\mathcal{R}_0$ and
 627 $I(0) = 100$ from 1990 to 2025 and truncate the time series to 2014–2025; if the
 628 epidemic becomes extinct before the end of simulation, we discard that simulation
 629 and start over from the intervention generation step. We then apply the window
 630 selection criteria described in the main text to compute the empirical resilience and
 631 compare it against the intrinsic resilience of the seasonally unforced system. We also
 632 compare this with the naive approach that uses the entire distance-from-attractor
 633 time series, starting from the maximum distance. We repeat this procedure 500
 634 times and quantify the correlation between empirical and intrinsic resilience estimates
 635 across two approaches.

Supplementary Figures

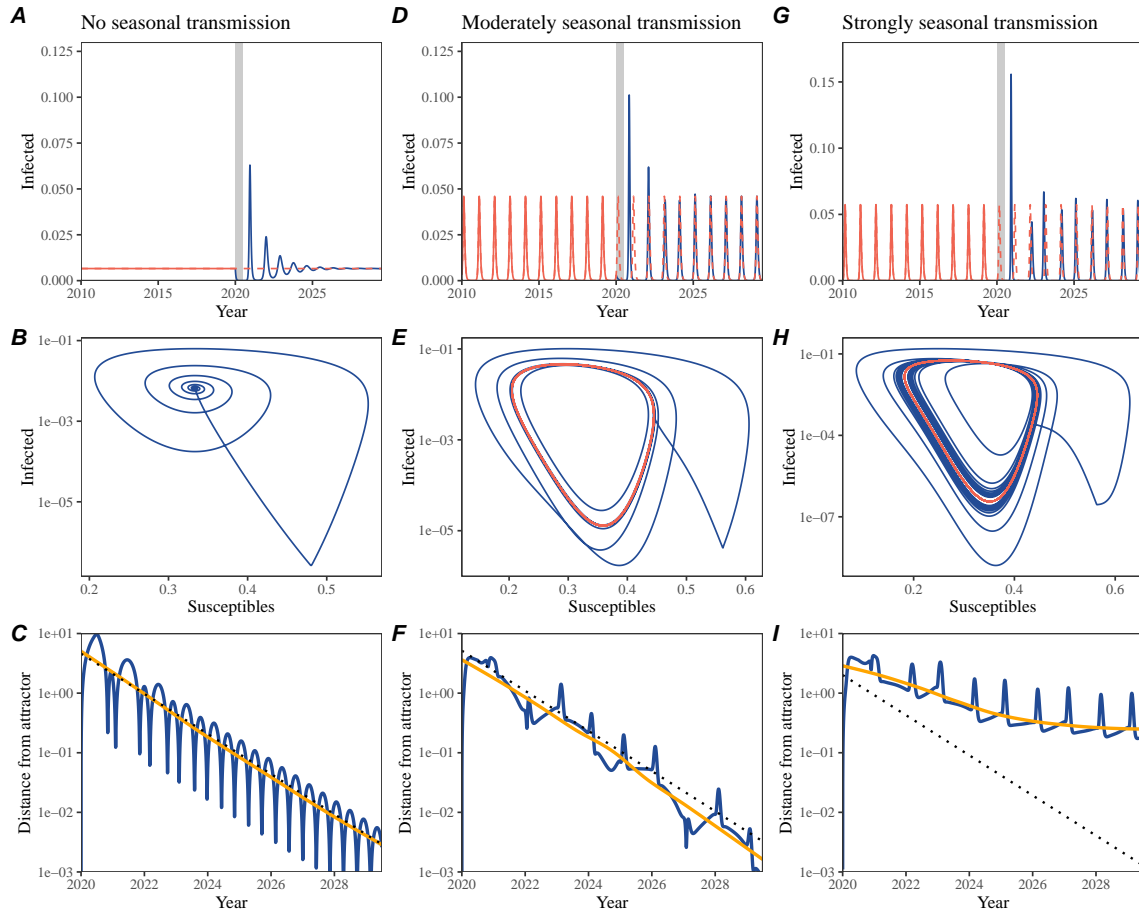


Figure S1: Impact of seasonal transmission on pathogen resilience. (A, D, G) Simulated epidemic trajectories using the SIRS model without seasonal forcing (A), with seasonal forcing of amplitude of 0.2 (D), and with seasonal forcing of amplitude of 0.2 (G). Red and blue solid lines represent epidemic dynamics before and after interventions are introduced, respectively. Red dashed lines represent counterfactual epidemic dynamics in the absence of interventions. Gray regions indicate the duration of interventions. (B, E, H) Phase plane representation of the corresponding model. Red and blue solid lines represent epidemic trajectories on an SI phase plane before and after interventions are introduced, respectively. (C, F, I) Changes in logged distance from attractor over time. Blue lines represent the logged distance from attractor. Orange lines represent the locally estimated scatterplot smoothing (LOESS) fits to the logged distance from attractor. Dotted lines are superimposed as a comparison to have the same slope as the intrinsic resilience of the seasonally unforced system.

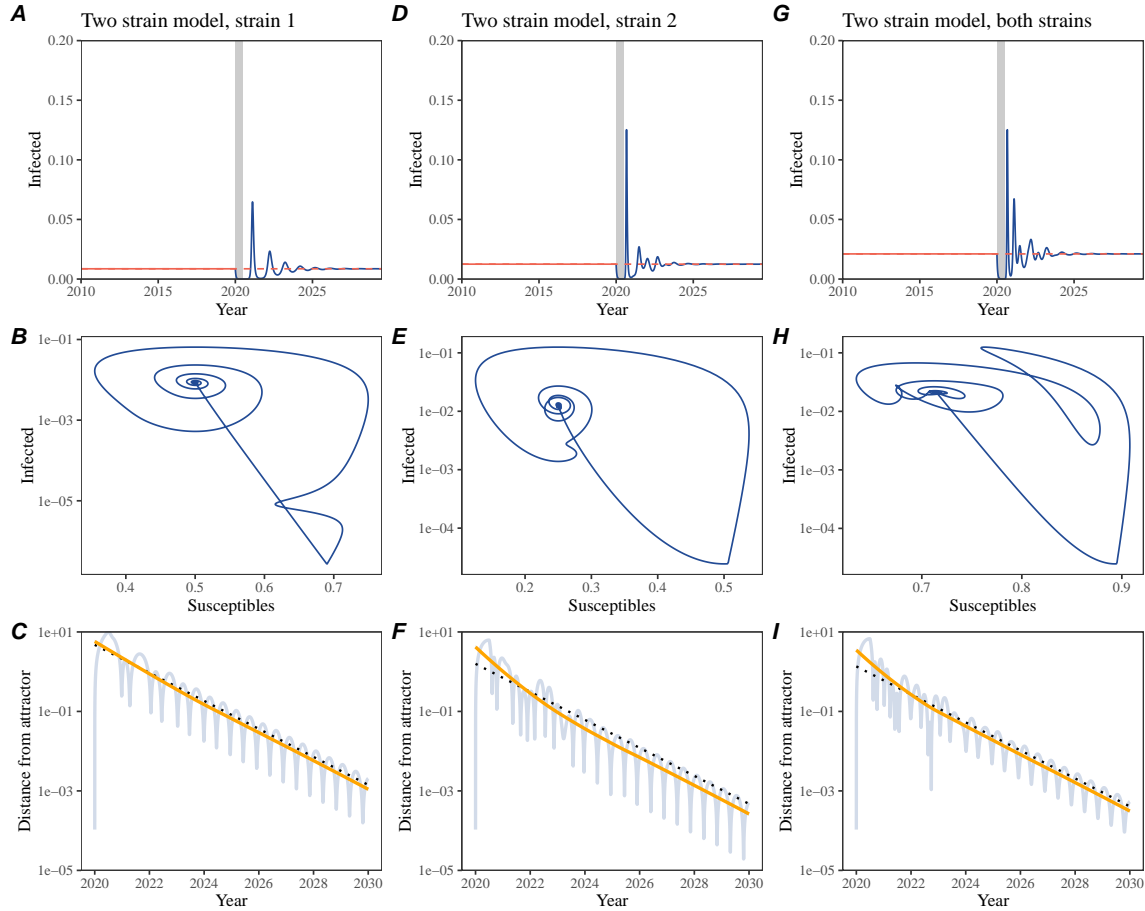


Figure S2: Conceptual framework for measuring pathogen resilience following NPIs for a multi-strain system without seasonal forcing. (A, D, G) Simulated epidemic trajectories using a multi-strain system without seasonal forcing. Red and blue solid lines represent epidemic dynamics before and after interventions are introduced, respectively. Red dashed lines represent counterfactual epidemic dynamics in the absence of interventions. Gray regions indicate the duration of interventions. (B, E, H) Phase plane representation of the corresponding model. Red and blue solid lines represent epidemic trajectories on an SI phase plane before and after interventions are introduced, respectively. (C, F, I) Changes in logged distance from attractor over time. Blue lines represent the logged distance from attractor. Orange lines represent the locally estimated scatterplot smoothing (LOESS) fits to the logged distance from attractor. Dotted lines are superimposed as a comparison to have the same slope as the intrinsic resilience of the seasonally unforced system.

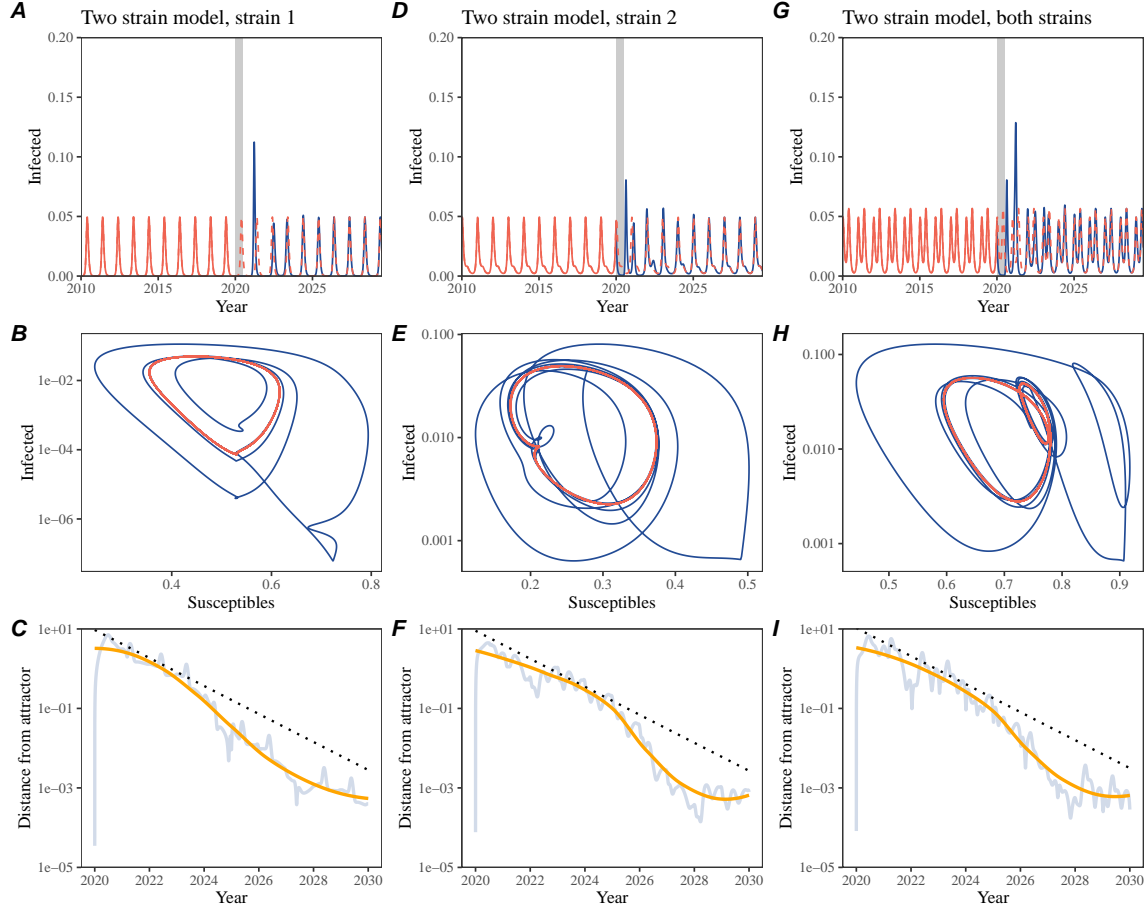


Figure S3: Conceptual framework for measuring pathogen resilience following NPIs for a multi-strain system with seasonal forcing. (A, D, G) Simulated epidemic trajectories using a multi-strain system with seasonal forcing (amplitude of 0.2). Red and blue solid lines represent epidemic dynamics before and after interventions are introduced, respectively. Red dashed lines represent counterfactual epidemic dynamics in the absence of interventions. Gray regions indicate the duration of interventions. (B, E, H) Phase plane representation of the corresponding model. Red and blue solid lines represent epidemic trajectories on an SI phase plane before and after interventions are introduced, respectively. (C, F, I) Changes in logged distance from attractor over time. Blue lines represent the logged distance from attractor. Orange lines represent the locally estimated scatterplot smoothing (LOESS) fits to the logged distance from attractor. Dotted lines are superimposed as a comparison to have the same slope as the intrinsic resilience of the seasonally unforced system.

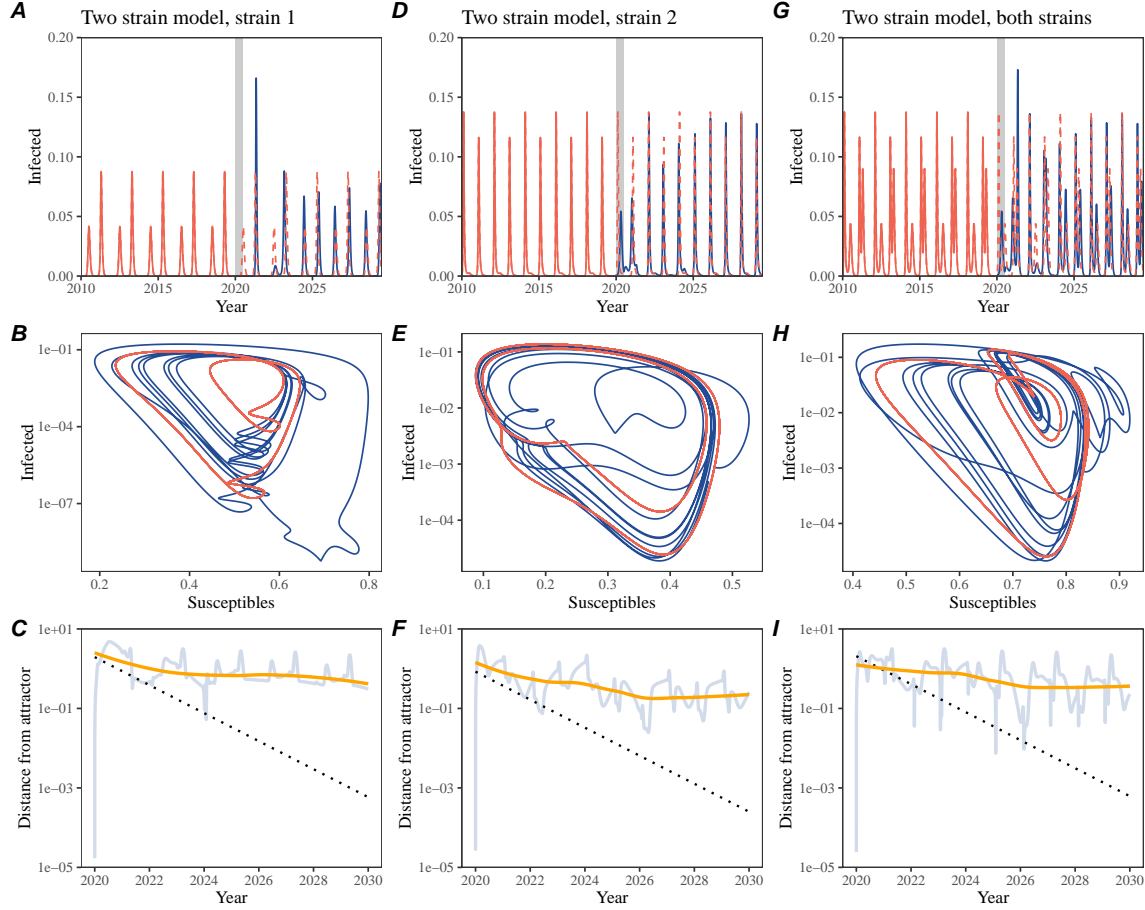


Figure S4: Conceptual framework for measuring pathogen resilience following NPIs for a multi-strain system with strong seasonal forcing. (A, D, G) Simulated epidemic trajectories using a multi-strain system with seasonal forcing (amplitude of 0.4). Red and blue solid lines represent epidemic dynamics before and after interventions are introduced, respectively. Red dashed lines represent counterfactual epidemic dynamics in the absence of interventions. Gray regions indicate the duration of interventions. (B, E, H) Phase plane representation of the corresponding model. Red and blue solid lines represent epidemic trajectories on an SI phase plane before and after interventions are introduced, respectively. (C, F, I) Changes in logged distance from attractor over time. Blue lines represent the logged distance from attractor. Orange lines represent the locally estimated scatterplot smoothing (LOESS) fits to the logged distance from attractor. Dotted lines are superimposed as a comparison to have the same slope as the intrinsic resilience of the seasonally unforced system.

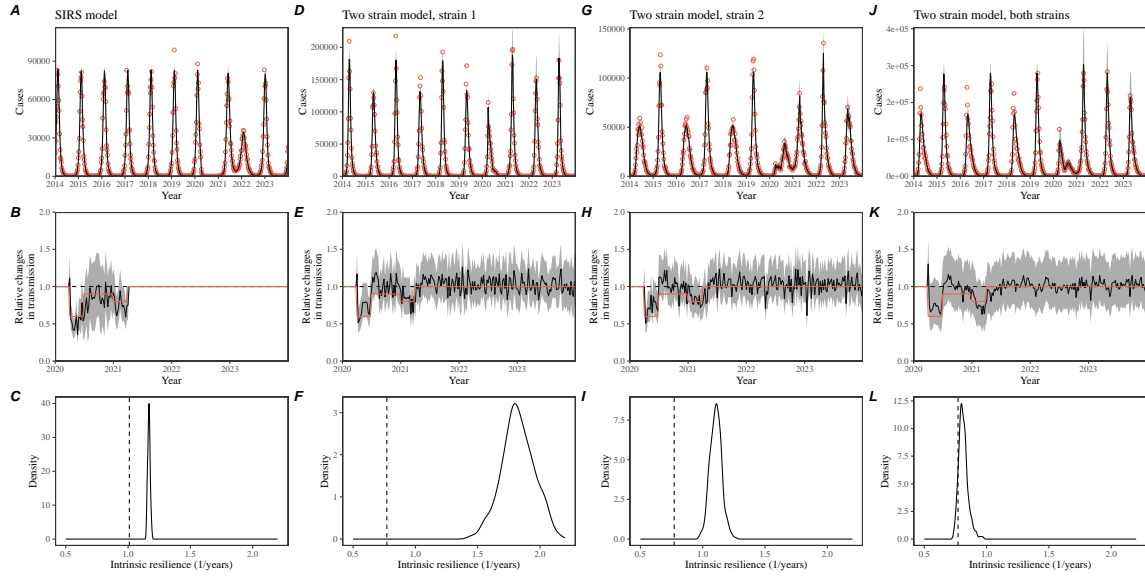


Figure S5: Mechanistic model fits to simulated data and inferred intrinsic resilience. (A, D, G, J) Simulated case time series from corresponding models (red) and SIRS model fits (black). (B, E, H, K) Assumed changes in transmission due to COVID-19 interventions (red) and estimated changes from the SIRS model (black). Solid lines and shaded regions represent fitted posterior median and 95% credible intervals. (C, F, I, L) True intrinsic resilience of the seasonally unforced system (vertical lines) and the posterior distribution of the inferred intrinsic resilience from the SIRS model (density plots).

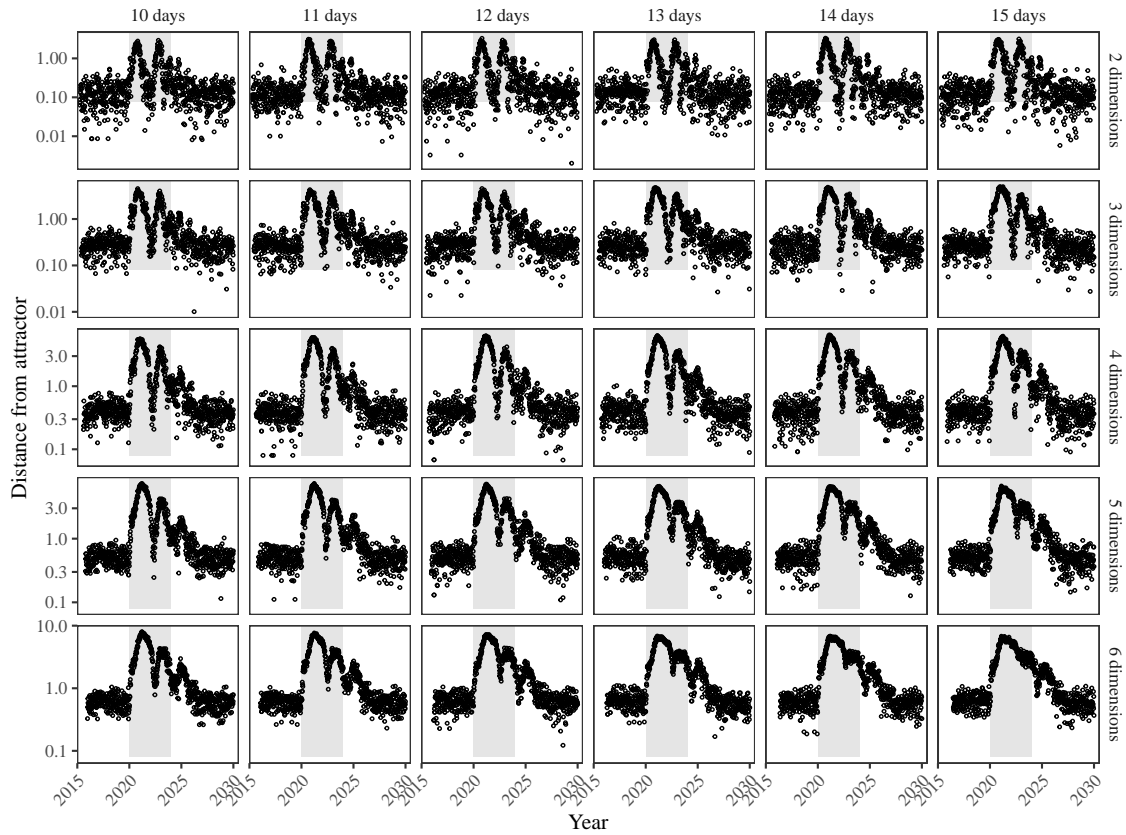


Figure S6: Sensitivity of the distance from attractor to choices about embedding lags and dimensions. Sensitivity analysis for the distance-from-attractor time series shown in Figure 3E in the main text by varying the embedding lag between 10–15 days and embedding dimensions between 2–6 dimensions.

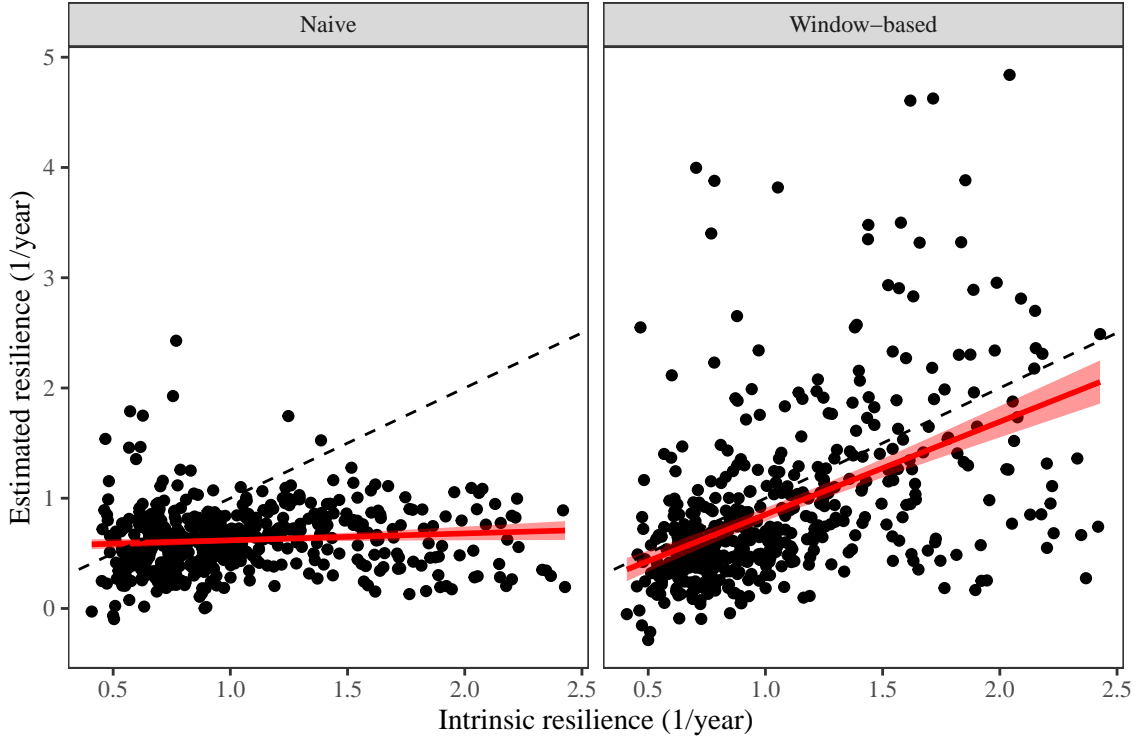


Figure S7: Impact of fitting window selection on the estimation of empirical resilience. We simulate 500 epidemics using stochastic SIRS model with randomly drawn parameters and randomly generated intervention impacts. For each simulation, we reconstruct the empirical attractor based on the approach outlined in Figure 3 and estimate the distance from attractor. The naive approach fits a linear regression on a log scale, starting from the maximum distance until the end of the time series. The window-based approach tries to select an appropriate window by smoothing the distance estimates and finding a time period when the smoothed time series crosses pre-determined threshold, relatively to the maximum distance; then, a linear regression is fitted by using the raw distance within this time period.

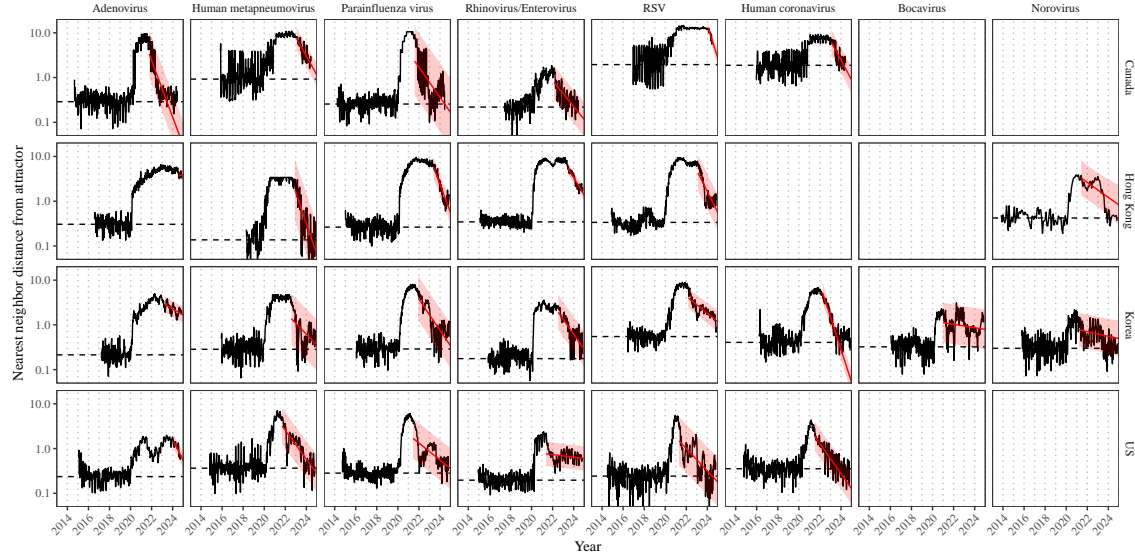


Figure S8: Estimated time series of distance from attractor for each pathogen across Canada, Hong Kong, Korea, and the US. Black lines represent the estimated distance from attractor. Red lines and shaded regions represent the linear regression fits and corresponding 95% confidence intervals. Dashed lines represent the average of the pre-pandemic nearest neighbor distances.

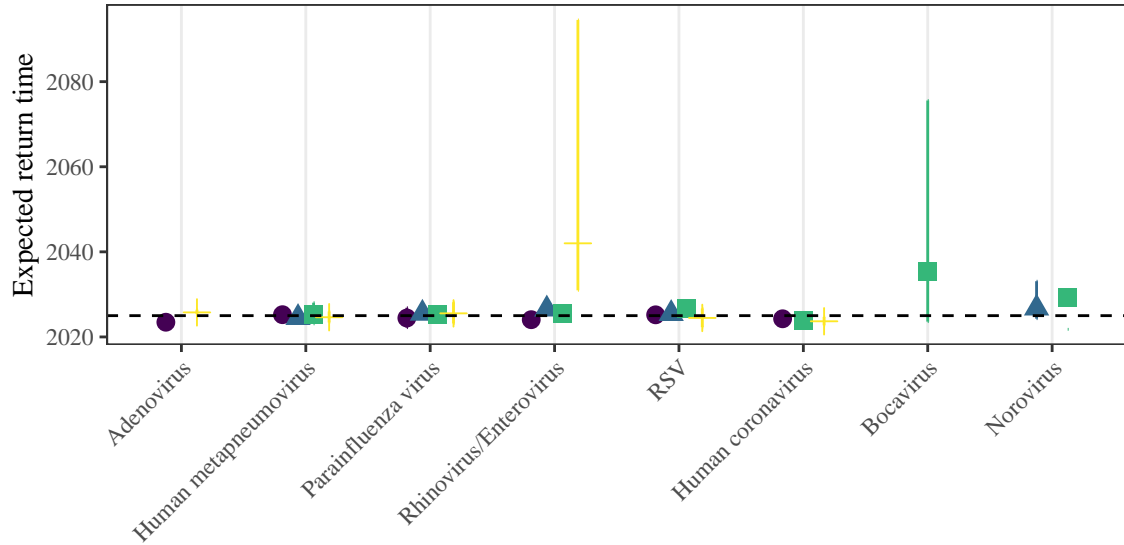


Figure S9: **Predicted timing of when each pathogen will return to their pre-pandemic cycles (zoomed out).** The dashed line in panel B indicates the end of 2024 (current observation time). Error bars represent 95% confidence intervals.

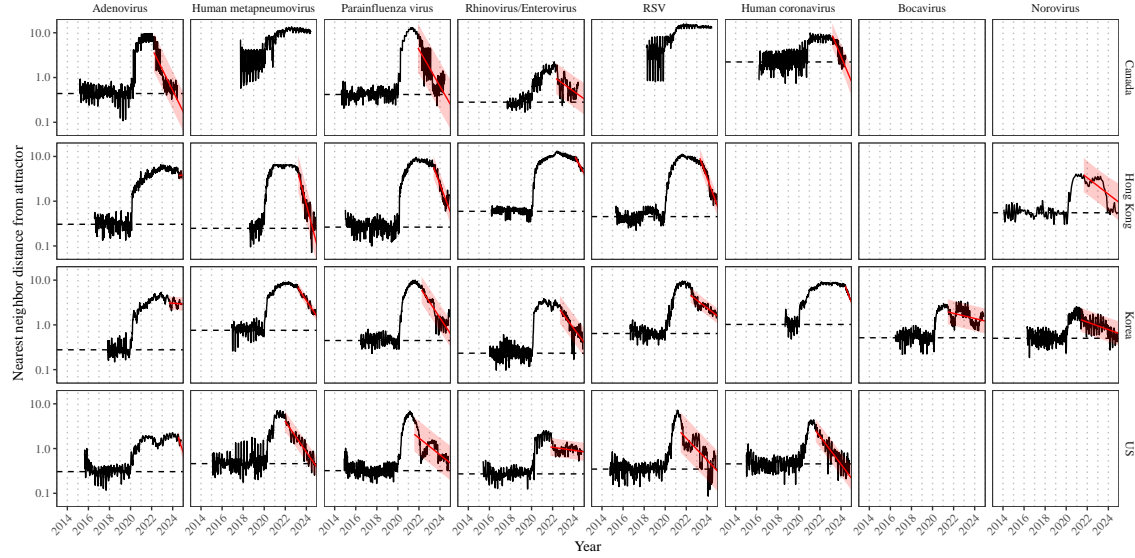


Figure S10: Estimated time series of distance from attractor for each pathogen across Canada, Hong Kong, Korea, and the US using higher embedding dimensions. Black lines represent the estimated distance from attractor. Red lines and shaded regions represent the linear regression fits and corresponding 95% confidence intervals. Dashed lines represent the average of the pre-pandemic nearest neighbor distances. A lower threshold is used for determining embedding dimensions with the false nearest neighbors approach, thereby yielding a higher embedding dimension.

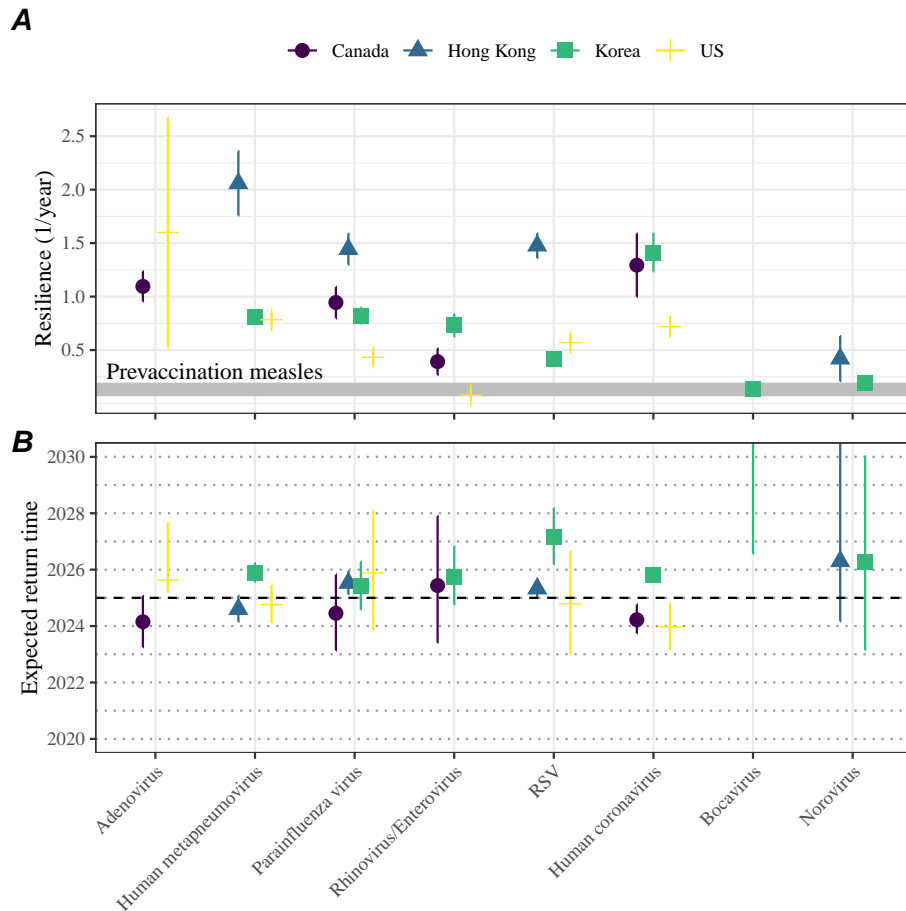


Figure S11: **Summary of resilience estimates using higher embedding dimensions.** (A) Estimated pathogen resilience. The gray horizontal line represents the intrinsic resilience of pre-vaccination measles dynamics. (B) Predicted timing of when each pathogen will return to their pre-pandemic cycles. The dashed line in panel B indicates the end of 2024 (current observation time). Error bars represent 95% confidence intervals. A lower threshold is used for determining embedding dimensions with the false nearest neighbors approach, thereby yielding a higher embedding dimension.

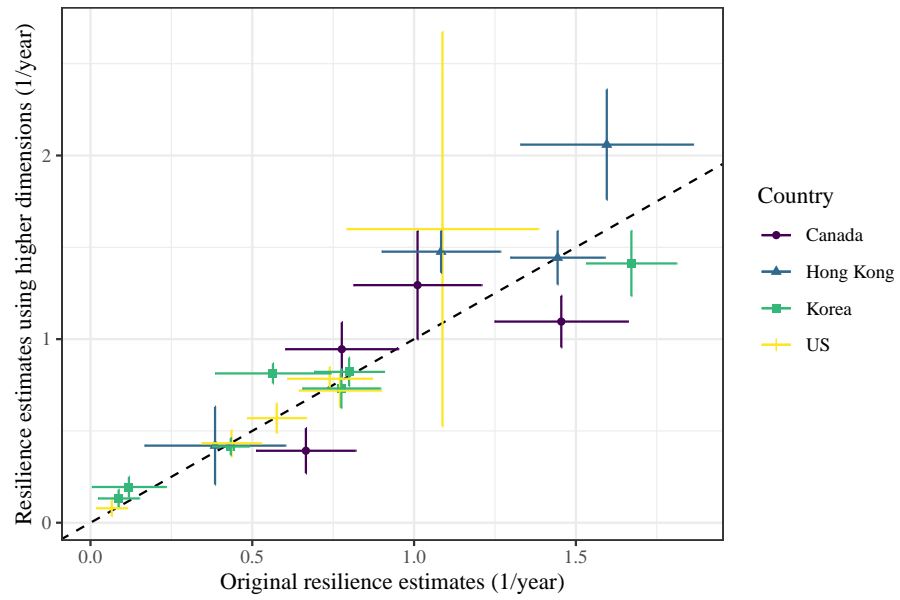


Figure S12: **Comparison of resilience estimates.** Each point represents a resilience estimate for a specific pathogen at a specific country. The x values represent the original resilience estimates presented in Figure 4. The y values represent the original resilience estimates presented in Supplementary Figure S11.

637 **References**

- 638 [1] Rachel E Baker, Sang Woo Park, Wenchang Yang, Gabriel A Vecchi, C Jessica E
639 Metcalf, and Bryan T Grenfell. The impact of COVID-19 nonpharmaceutical
640 interventions on the future dynamics of endemic infections. *Proceedings of the*
641 *National Academy of Sciences*, 117(48):30547–30553, 2020.
- 642 [2] Gabriela B Gomez, Cedric Mahé, and Sandra S Chaves. Uncertain effects of the
643 pandemic on respiratory viruses. *Science*, 372(6546):1043–1044, 2021.
- 644 [3] Mihaly Koltai, Fabienne Krauer, David Hodgson, Edwin van Leeuwen, Marina
645 Treskova-Schwarzbach, Mark Jit, and Stefan Flasche. Determinants of RSV
646 epidemiology following suppression through pandemic contact restrictions. *Epi-*
647 *demics*, 40:100614, 2022.
- 648 [4] Sang Woo Park, Brooklyn Noble, Emily Howerton, Bjarke F Nielsen, Sarah
649 Lentz, Lilliam Ambroggio, Samuel Dominguez, Kevin Messacar, and Bryan T
650 Grenfell. Predicting the impact of non-pharmaceutical interventions against
651 COVID-19 on *Mycoplasma pneumoniae* in the United States. *Epidemics*,
652 49:100808, 2024.
- 653 [5] Amanda C Perofsky, Chelsea L Hansen, Roy Burstein, Shanda Boyle, Robin
654 Prentice, Cooper Marshall, David Reinhart, Ben Capodanno, Melissa Truong,
655 Kristen Schwabe-Fry, et al. Impacts of human mobility on the citywide trans-
656 mission dynamics of 18 respiratory viruses in pre-and post-COVID-19 pandemic
657 years. *Nature communications*, 15(1):4164, 2024.
- 658 [6] Eric J Chow, Timothy M Uyeki, and Helen Y Chu. The effects of the COVID-19
659 pandemic on community respiratory virus activity. *Nature Reviews Microbiol-*
660 *ogy*, 21(3):195–210, 2023.
- 661 [7] Stephen M Kissler, Christine Tedijanto, Edward Goldstein, Yonatan H Grad,
662 and Marc Lipsitch. Projecting the transmission dynamics of SARS-CoV-2
663 through the postpandemic period. *Science*, 368(6493):860–868, 2020.
- 664 [8] Rachel E Baker, Chadi M Saad-Roy, Sang Woo Park, Jeremy Farrar, C Jessica E
665 Metcalf, and Bryan T Grenfell. Long-term benefits of nonpharmaceutical inter-
666 ventions for endemic infections are shaped by respiratory pathogen dynamics.
667 *Proceedings of the National Academy of Sciences*, 119(49):e2208895119, 2022.
- 668 [9] John-Sebastian Eden, Chisha Sikazwe, Ruopeng Xie, Yi-Mo Deng, Sheena G
669 Sullivan, Alice Michie, Avram Levy, Elena Cutmore, Christopher C Blyth,
670 Philip N Britton, et al. Off-season RSV epidemics in Australia after easing
671 of COVID-19 restrictions. *Nature communications*, 13(1):2884, 2022.
- 672 [10] Stuart L Pimm. The structure of food webs. *Theoretical population biology*,
673 16(2):144–158, 1979.

- 674 [11] Michael G Neubert and Hal Caswell. Alternatives to resilience for measuring
675 the responses of ecological systems to perturbations. *Ecology*, 78(3):653–665,
676 1997.
- 677 [12] Lance H Gunderson. Ecological resilience—in theory and application. *Annual
678 review of ecology and systematics*, 31(1):425–439, 2000.
- 679 [13] Vasilis Dakos and Sonia Kéfi. Ecological resilience: what to measure and how.
680 *Environmental Research Letters*, 17(4):043003, 2022.
- 681 [14] Floris Takens. Detecting strange attractors in turbulence. In *Dynamical Sys-
682 tems and Turbulence, Warwick 1980: proceedings of a symposium held at the
683 University of Warwick 1979/80*, pages 366–381. Springer, 2006.
- 684 [15] Alan Hastings, Karen C Abbott, Kim Cuddington, Tessa Francis, Gabriel Gell-
685 ner, Ying-Cheng Lai, Andrew Morozov, Sergei Petrovskii, Katherine Scran-
686 ton, and Mary Lou Zeeman. Transient phenomena in ecology. *Science*,
687 361(6406):eaat6412, 2018.
- 688 [16] Matthew B Kennel, Reggie Brown, and Henry DI Abarbanel. Determining
689 embedding dimension for phase-space reconstruction using a geometrical con-
690 struction. *Physical review A*, 45(6):3403, 1992.
- 691 [17] Eugene Tan, Shannon Algar, Débora Corrêa, Michael Small, Thomas Stemler,
692 and David Walker. Selecting embedding delays: An overview of embedding
693 techniques and a new method using persistent homology. *Chaos: An Interdis-
694 ciplinary Journal of Nonlinear Science*, 33(3), 2023.
- 695 [18] Samit Bhattacharyya, Per H Gesteland, Kent Korgenski, Ottar N Bjørnstad,
696 and Frederick R Adler. Cross-immunity between strains explains the dynamical
697 pattern of paramyxoviruses. *Proceedings of the National Academy of Sciences*,
698 112(43):13396–13400, 2015.
- 699 [19] Bryan T Grenfell, Ottar N Bjørnstad, and Bärbel F Finkenstädt. Dynamics of
700 measles epidemics: scaling noise, determinism, and predictability with the TSIR
701 model. *Ecological monographs*, 72(2):185–202, 2002.
- 702 [20] Virginia E Pitzer, Cécile Viboud, Wladimir J Alonso, Tanya Wilcox, C Jessica
703 Metcalf, Claudia A Steiner, Amber K Haynes, and Bryan T Grenfell. Environ-
704 mental drivers of the spatiotemporal dynamics of respiratory syncytial virus in
705 the United States. *PLoS pathogens*, 11(1):e1004591, 2015.
- 706 [21] Katharine R Dean, Fabienne Krauer, Lars Walløe, Ole Christian Lingjærde, Bar-
707 Barbara Bramanti, Nils Chr Stenseth, and Boris V Schmid. Human ectoparasites
708 and the spread of plague in Europe during the Second Pandemic. *Proceedings
709 of the National Academy of Sciences*, 115(6):1304–1309, 2018.

- 710 [22] Margarita Pons-Salort and Nicholas C Grassly. Serotype-specific immunity
711 explains the incidence of diseases caused by human enteroviruses. *Science*,
712 361(6404):800–803, 2018.
- 713 [23] Sarah Cobey and Edward B Baskerville. Limits to causal inference with state-
714 space reconstruction for infectious disease. *PloS one*, 11(12):e0169050, 2016.
- 715 [24] Edward Goldstein, Sarah Cobey, Saki Takahashi, Joel C Miller, and Marc Lip-
716 sitch. Predicting the epidemic sizes of influenza A/H1N1, A/H3N2, and B: a
717 statistical method. *PLoS medicine*, 8(7):e1001051, 2011.
- 718 [25] Bob Carpenter, Andrew Gelman, Matthew D Hoffman, Daniel Lee, Ben
719 Goodrich, Michael Betancourt, Marcus A Brubaker, Jiqiang Guo, Peter Li,
720 and Allen Riddell. Stan: A probabilistic programming language. *Journal of
721 statistical software*, 76, 2017.
- 722 [26] Stan Development Team. RStan: the R interface to Stan, 2024. R package
723 version 2.32.6.